Analytical Model for Non-linear $M-\theta$ Relationships of Dowel-Type Timber Connections Exposed to Fire

Yukito Nakayama ⓘ*, Graduate School of Science and Engineering, Chiba University, Chiba, Japan*

Takayuki Kikuchi ⓘ, *Faculty of Engineering, Chiba University, Chiba, Japan*

Marina Totsuka ⓘ *and Takeo Hirashima* ⓘ, *Graduate School of Engineering, Chiba University, Chiba, Japan*

Abstract. Recent experimental evidence has shown that wood–steel–wood dowel-type connections exhibit a semi-rigid behaviour even after 90 min of fire exposure. Because a semi-rigid behaviour influences the bending moment distribution among structural members, considering the moment–rotation relationships within frame analyses in which structural members are modelled as beam elements can enable a realistic fire response analysis that is significantly simpler than the three-dimensional finite element method. This study proposes an analytical methodology that accounts for the thermo-mechanical behaviour of timber and dowels, enabling the simulation of the non-linear moment–rotation relationships under fire conditions. The proposed analytical model divides dowels into a series of elements on an elastoplastic foundation and performs a direct stiffness method in a time-incremental procedure using an element stiffness matrix derived from beam-on-elastic-foundation theory. This study also presents the results of load-carrying tests on timber frames with dowel-type connections performed under ambient and fire conditions. The analytical results were consistent with the fire test results. Additionally, the analyses were also performed under three conditions in which the dowels were rigid, linear elastic, and elastoplastic bodies. These three results converged to the same value after 65 min of heating, which suggests that the ultimate states of beams with dowel-type connections exposed to fire can be modelled by assuming that dowels are rigid bodies.

Keywords: Analytical modelling, Dowel-type timber connections, Moment–rotation relationships, Fire

1. Introduction

The use of mass timber as a primary building material has seen a gradual increase over the past few decades owing to its sustainability and aesthetic appearance. Among the various connection types used in mass timber construction, the wood–steel–wood (WSW) dowel-type connection is one of the most prevalent, which

---

*Correspondence should be addressed to: Yukito Nakayama, E-mail: yukiton@chiba-u.jp

consists of multiple cylindrical dowels penetrating holes pre-drilled in the timber and a slotted-in steel plate. Due to their semi-rigidity, the moment–rotation response of dowel-type connections exposed to fire falls between fully rigid and pinned responses [1]. Furthermore, recent experimental evidence has shown that dowel-type connections wherein the dowels are fire-protected by wooden plugs can resist both shear and bending stresses for longer than 90 min of fire exposure [2, 3]. Thus, considering the moment–rotation relationships in frame analyses in which structural members are modelled as beam elements, such as [4], will enable a realistic fire response analysis that is significantly simpler than the well-used three-dimensional finite element method (FEM). This methodology has been adopted for steel structures with the concept of the so-called "component method" [5, 6], which mechanically models a joint as an assembly of springs that exhibit load–displacement responses of the joineries; however, the application of the component method to timber structures is unprecedented. Due to limited experimental and numerical studies, dowel-type connections are generally considered pins in the structural fire design of timber structures.

Under ambient conditions, beam-on-elastic-foundation (BOEF) theory is often utilized to model dowel-type connections, enabling the consideration of stress distribution along dowels arising from their deformation. Kuenzi adopted the BOEF theory to theoretically describe the linear elastic deformation of a nail and bolt in timber [7]. Hirai and Sawada subsequently implemented the BOEF theory to evaluate the load-slip relationship of a bolt within the elastic range [8, 9]. Analytical models employing the BOEF theory have also been utilized for the elastic deformation of a screw [10] and a dowel-type fastener in WSW connections [11]. Furthermore, Tsujino and Hirai combined the BOEF theory with an incremental FEM to address the elastoplastic deformation problem of a fastener in timber [12–14]. Other studies that attempted to analyse the elastoplastic behaviour of a fastener can be found in the literature [15, 16]. These single-fastener models can simulate the load-slip responses, making them easily applicable to mechanical models for moment–rotation relationships of dowel-type connections. Yasuda et al. applied a single fastener model to analyse elastoplastic moment–rotation relationships of dowel-type connections at ambient temperature [17]. Awaludin et al. expressed load-slip relationships in an exponential form and analysed the elastoplastic moment–rotation relationships under ambient temperature [18]. Guidance is also given by the Japanese *Design Manual for Engineered Timber Joints* [19] on how to evaluate moment–rotation relationships of dowel-type connections in the structural design of timber structures under ambient conditions. In recent years, there have been some studies on the fire behaviour of single fasteners. One notable example is the component model proposed by Cachim and Franssen [20], which successfully simulates the thermo-mechanical behaviour of single fasteners under fire loading. However, limited studies have yet been performed on moment–rotation relationships of dowel-type connections exposed to fire.

Under fire conditions, most studies were focused on the behaviour of dowel-type connections loaded parallel or perpendicular to the grain. Erchinger et al. conducted fire tests on multiple shear dowel-type connections under tension and developed a design model based on the reduced cross-section method to calculate

the load-bearing capacity of the tested connections [21]. Audebert et al. employed a three-dimensional FEM to simulate the fire behaviour of dowel-type connections loaded parallel [22–24] and perpendicular [25] to the grain. Palma et al. also conducted an extensive experimental program on dowel-type connections loaded perpendicular to the grain with various dowel arrangements [26]. Moreover, there have been several attempts to predict the fire resistance of dowel-type connections under fire loading by combining Johansen's yield model with a three-dimensional heat transfer analysis [27–29]. These investigations have implied that the charring of wood side members shortens the effective length of the dowel. This causes the yield mode to transition to Mode I at the ultimate state of fire, which is determined only by the embedding failure of the timber. In the past few years, there has been a growing interest in investigating the fire behaviour of dowel-type connections when subjected to bending moments. Dhima et al. conducted a fire experiment on dowel-type connections in bending and used a three-dimensional FEM to simulate both heat transfer and the thermo-mechanical behaviour of the tested connections [30]. Li et al. and Luo et al. have presented an analytical model to predict the fire resistance of dowel-type connections subjected to bending moments [31, 32]. Luo et al. have utilized a three-dimensional FEM to simulate the fire behaviour of dowel-type connections under both shear force and bending moments [33]. However, these approaches are not compatible with fire response frame analyses that use beam elements. To the best of our knowledge, no model based on the component method has been developed so far for the moment–rotation relationships of dowel-type connections under fire conditions.

This paper presents an analytical methodology that can simulate non-linear moment–rotation relationships of dowel-type connections exposed to fire (non-linear $M - \theta$ model). The non-linear $M - \theta$ model is a mechanical model consisting of springs that exhibit non-linear load-slip relationships of dowels, accounting for stress distributions along dowels arising from their deformation. This paper first outlines the theoretical model for linear elastic moment–rotation relationships [19] (a linear $M - \theta$ model), which serves as the basis for the non-linear $M - \theta$ model. Following that, the analytical framework for the non-linear $M - \theta$ model is presented. This study also includes the results of load-carrying tests on timber frames with dowel-type connections, performed under ambient and fire conditions, and compares the results obtained using the linear and non-linear $M - \theta$ models with the experimental results to validate the models.

The superscripts and subscripts used in this paper are defined as follows:

Superscripts

T	Time step number
c	Convergence step number for determination of rotation centre.

Subscripts

i	Element number
j	Node number
m	Dowel number
α	Angle to grain (the definition range is $[0, 2\pi]$, 0 when parallel to grain)

2. Linear $M - \theta$ Model at Ambient Temperature

2.1. Linear $M - \theta$ Relationships

When a bending moment acts on a WSW dowel-type connection, the dowels contact the slotted-in steel plate, thereby bearing the reaction forces equivalent to the bending moment from the contact point, as shown in Fig. 1. The relationship between the reaction force applied to the dowel and the displacement at the loading point is generally called the load–slip relationship, which exhibits almost linear behaviour in the elastic range at ambient temperature. Thus, dowel-type connections can be modelled simply in two dimensions by representing the load–slip relationships of dowels as linear springs. Each spring's stiffness corresponds to the initial stiffness of the load–slip relationship (slip modulus) that accounts for the elastic deformation of both the dowel and timber. The assembly rotation, θ, causes the springs to elongate or compress proportionally to their distance from the rotation centre. The bending moment in the assembly, M, results from the reaction force of each spring, which is determined by the product of the spring elongation or compression and the spring constant. Figure 2 illustrates an example of a spring model for dowel-type connections when the dowels are arranged in a vertical line. As shown in Fig. 3, the linear elastic $M - \theta$ relationships of the dowel-type connections at ambient temperature [19] are expressed as follows:

$$M = \left(\sum_{m=1}^{n_d} K_{\alpha_m} \cdot r_m^2 \right) \theta \tag{1}$$

where M denotes the bending moment acting on the connection, θ denotes the rotation of the connection, n_d denotes the total number of dowels, α_m denotes the slip angle of dowel m to the grain, $K_{\alpha m}$ denotes the slip modulus at the angle α_m to the grain, and r_m denotes the distance from the rotation centre to dowel m. The rotation centre under ambient conditions always coincides with the centroid point of the dowel arrangement. Thus, r_m can be expressed as:

$$r_m = \sqrt{X_m^2 + Y_m^2} \tag{2}$$

where X_m denotes the x-coordinate of dowel m from the centroid point, and Y_m denotes the y-coordinate of dowel m from the centroid point. The slip angle of dowel m to the grain, α_m, can be calculated using:

$$\alpha_m = \begin{cases} \dfrac{\pi}{2} - \tan^{-1}\left(\dfrac{Y_m}{X_m}\right) & (X_m > 0) \\[2mm] \dfrac{3}{2}\pi - \tan^{-1}\left(\dfrac{Y_m}{X_m}\right) & (X_m < 0) \\[2mm] 0 & (X_m = 0 \text{ and } Y_m > 0) \\[2mm] \pi & (X_m = 0 \text{ and } Y_m < 0) \end{cases} \tag{3}$$
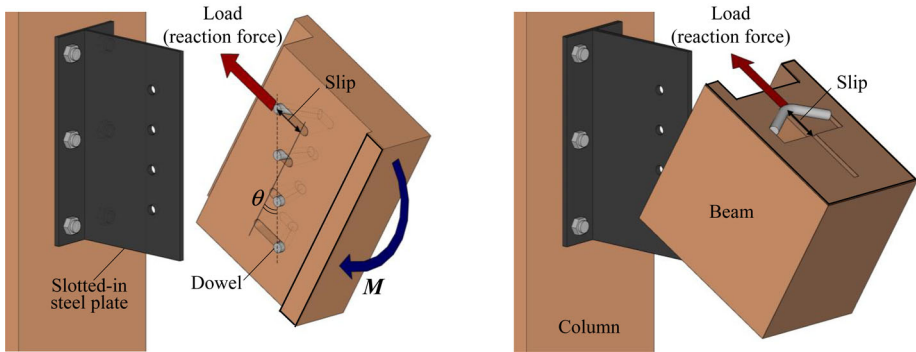
Figure 1. **Resistance mechanism of dowel-type connections subjected to a bending moment.**
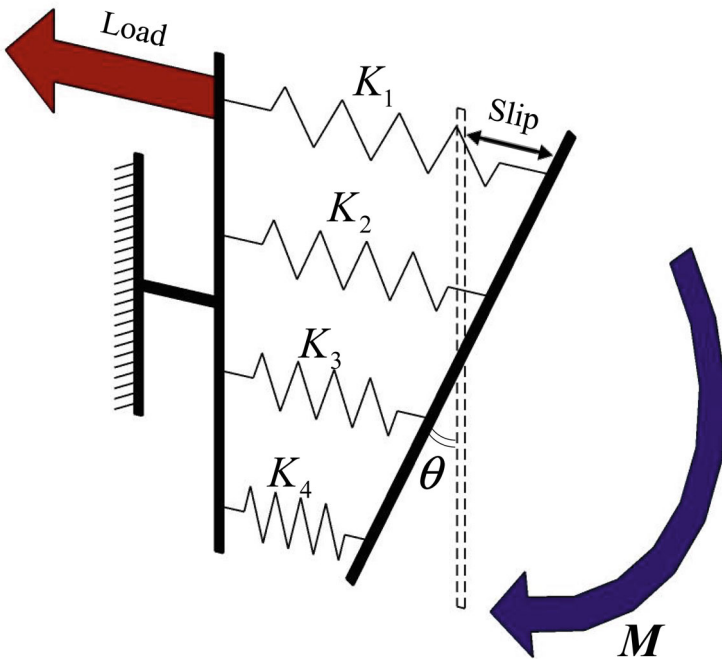

Figure 2. **Example of mechanical model for dowel-type connections.**

2.2. Slip Modulus

The objective of this section is to derive the slip modulus K_{α_m} using the BOEF theory. The bending moment distribution along a dowel, $M(x)$, can be expressed using the deflection curve of the dowel, $y(x)$, that is:
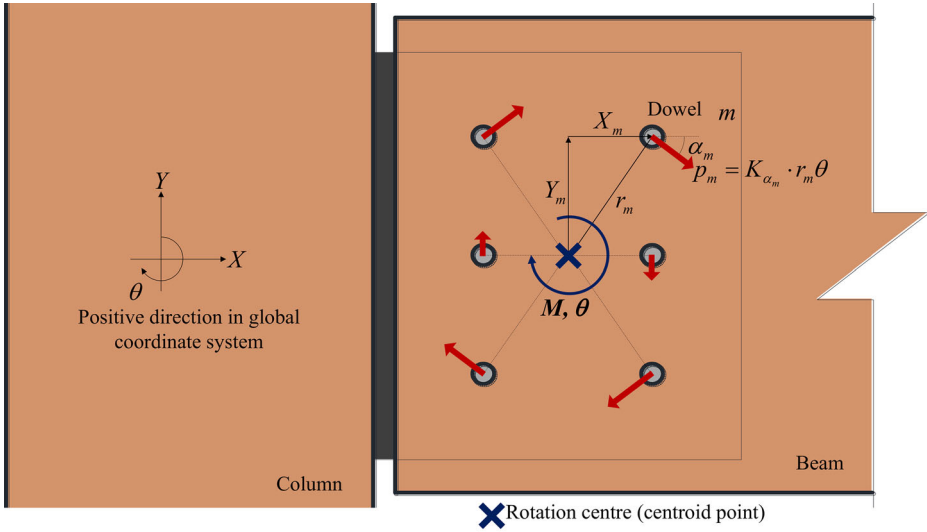
Figure 3. Linear M − θ model.

$$M(x) = -EI \frac{d^2 y(x)}{dx^2} \tag{4}$$

where *EI* denotes the bending stiffness of the dowel. When a distributed load is acting on the dowel, the following relationship exists between the bending moment, the shear force, $Q(x)$, and the distributed load, $q(x)$:

$$\frac{d^2 M(x)}{dx^2} = \frac{dQ(x)}{dx} = -q(x) \tag{5}$$

Substituting Eq. (5) into (4) gives the following differential equation:

$$EI \frac{d^4 y(x)}{dx^4} = q(x) \tag{6}$$

According to the BOEF theory, the distributed load applied to the dowel from the elastic foundation $q(x)$ is assumed to be proportional to the deflection, which is $-k_\alpha d \cdot y(x)$. Thus, the deflection of the dowel $y(x)$ satisfies the differential equation:

$$EI \frac{d^4 y(x)}{dx^4} + k_\alpha d \cdot y(x) = 0 \tag{7}$$

where k_α denotes the embedding stiffness at the angle of α to the grain, and d denotes the dowel diameter. Assuming that the general solution of Eq. (7) is $y(x) = e^{bx}$, substituting $y(x) = e^{bx}$ into Eq. (7) gives:

$$EI \cdot b^4 + k_\alpha d = 0 \tag{8}$$

Thus, the constant b is expressed as:

$$b = \pm \sqrt[4]{k_\alpha d / 4EI}(1 \pm i) \tag{9}$$

Substituting Eq. (9) into $y(x) = e^{bx}$ gives the general solution of Eq. (7), which is:

$$y(x) = e^{\lambda_\alpha x}[A\cos(\lambda_\alpha x) + B\sin(\lambda_\alpha x)] + e^{-\lambda_\alpha x}[C\cos(\lambda_\alpha x) + D\sin(\lambda_\alpha x)] \tag{10}$$

where A, B, C, and D are constants of integration and λ_α stands for $\sqrt[4]{k_\alpha d / 4EI}$. For simplicity, the axial force within the dowel is ignored. As shown in Fig. 4, the boundary conditions of the dowel are:

$$\dddot{y}(0) = 0, \; \ddot{y}(0) = 0, \; \dot{y}(L/2) = 0, \; \text{and} \; \ddot{y}(L/2) = -p/2EI \tag{11}$$

where L is the dowel length and p is the reaction force. Thus, the integration constants that satisfy the boundary conditions above are:

$$A = \frac{\left(3 + e^{\lambda_\alpha L}\right)\cos(\lambda_\alpha L/2) + \left(1 + e^{\lambda_\alpha L}\right)\sin(\lambda_\alpha L/2)}{4k_\alpha d \cdot e^{\lambda_\alpha L/2}[\sinh(\lambda_\alpha L) + \sin(\lambda_\alpha L)]} p\lambda_\alpha$$

and

$$B = D = \frac{\left(1 - e^{\lambda_\alpha L}\right)\cos(\lambda_\alpha L/2) + \left(1 + e^{\lambda_\alpha L}\right)\sin(\lambda_\alpha L/2)}{4k_\alpha d \cdot e^{\lambda_\alpha L/2}[\sinh(\lambda_\alpha L) + \sin(\lambda_\alpha L)]} p\lambda_\alpha$$

$$C = \frac{\left(1 + 3e^{\lambda_\alpha L}\right)\cos(\lambda_\alpha L/2) - \left(1 + e^{\lambda_\alpha L}\right)\sin(\lambda_\alpha L/2)}{4k_\alpha d \cdot e^{\lambda_\alpha L/2}[\sinh(\lambda_\alpha L) + \sin(\lambda_\alpha L)]} p\lambda_\alpha \tag{12}$$

Using the constants of integration defined above, the deflection of any point of the dowel can be calculated using Eq. (10). The deflection at the contact point $x = L/2$ is:

$$y(L/2) = e^{\lambda_\alpha \frac{L}{2}}\left[A\cos\left(\lambda_\alpha \frac{L}{2}\right) + B\sin\left(\lambda_\alpha \frac{L}{2}\right)\right] + e^{-\lambda_\alpha \frac{L}{2}}\left[C\cos\left(\lambda_\alpha \frac{L}{2}\right) + D\sin\left(\lambda_\alpha \frac{L}{2}\right)\right]$$
$$= \frac{\lambda_\alpha}{2k_\alpha d} \cdot \frac{\cosh(\lambda_\alpha L) + \cos(\lambda_\alpha L) + 2}{\sinh(\lambda_\alpha L) + \sin(\lambda_\alpha L)} \cdot p \tag{13}$$

Because $y(L/2)$ coincides with the slip caused by the reaction force, the slip modulus can be obtained by:
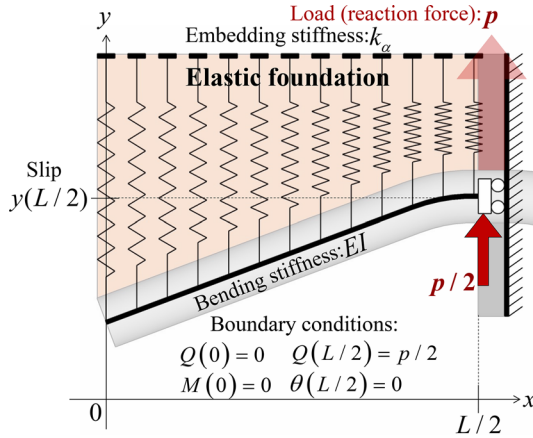
Figure 4. Model of a dowel on an elastic foundation.

$$K_\alpha = \frac{p}{y(L/2)} = \frac{2k_\alpha d}{\lambda_\alpha} \cdot \frac{\sinh(\lambda_\alpha L) + \sin(\lambda_\alpha L)}{\cosh(\lambda_\alpha L) + \cos(\lambda_\alpha L) + 2} \tag{14}$$

Due to the anisotropic nature of timber, slip modulus K_α depends on the angle to the grain. The slip modulus at the angle of α_m to the grain can be obtained using the well-known Hankinson's equation:

$$K_{\alpha_m} = \frac{K_{a=0} \cdot K_{\alpha=\pi/2}}{K_{a=0} \cdot \sin^2 \alpha_m + K_{\alpha=\pi/2} \cdot \cos^2 \alpha_m} \tag{15}$$

where $K_{a=0}$ denotes the slip modulus calculated using the embedding stiffness parallel to the grain, $k_{a=0}$, and $K_{a=\pi/2}$ denotes the slip modulus calculated using the embedding stiffness perpendicular to the grain, $k_{\alpha=\pi/2}$.

3. Non-linear $M - \theta$ Model at High Temperature

3.1. General Approach

Under fire exposure, the load–slip relationships exhibit nonlinearity because the mechanical properties of timber and steel vary with heating time. As temperature distribution occurs along the axial direction of the dowel, material properties also exhibit distribution in the axial direction under fire conditions. In addition, when the temperature of each dowel within a connection differs, the rotation centre shifts with heating time. This chapter introduces the non-linear $M - \theta$ model that can take these phenomena into account.

The non-linear load–slip relationships are represented as non-linear springs in the non-linear $M - \theta$ model, as shown in Fig. 5. Within a given time step, t, the
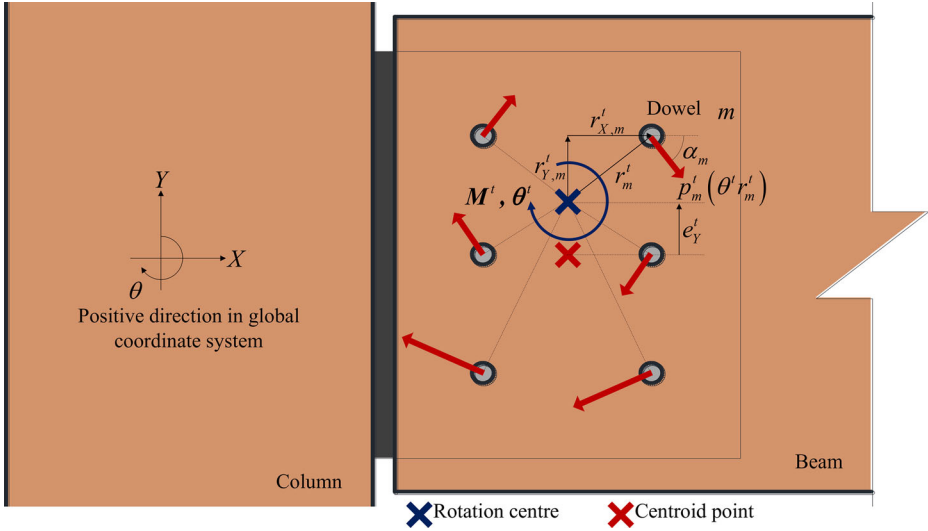
Figure 5. **Non-linear $M - \theta$ model.**

relationship between the current bending moment, M^t, and rotation, θ^t, is given by:

$$M^t = \sum_{m=1}^{n_d} p_m^t \left(\theta^t r_m^t \right) \cdot r_m^t \tag{16}$$

where r_m^t denotes the current distance from the rotation centre to dowel m and $\theta^t r_m^t$ denotes the current slip of dowel m. r_m^t can be calculated using:

$$r_m^t = \sqrt{{r_{X,m}^t}^2 + {r_{Y,m}^t}^2} \tag{17}$$

where $r_{X,m}^t$ denotes the current x-coordinate of dowel m from the rotation centre, and $r_{Y,m}^t$ denotes the current y-coordinate of dowel m from the rotation centre. Because the rotation centre position varies with the heating time, $r_{X,m}^t$ and $r_{Y,m}^t$ must be updated at each time step using:

$$r_{X,m}^t = X_m - e_X^t \approx X_m \text{ and } r_{Y,m}^t = Y_m - e_Y^t, \tag{18}$$

where X_m denotes the X-coordinate of dowel m from the centroid point, Y_m denotes the Y-coordinate of dowel m from the centroid point, e_X^t denotes the current X-coordinate of the rotation centre from the centroid point, and e_Y^t denotes the current Y-coordinate of the rotation centre from the centroid point. It should be noted that the symbol "e" denotes Napier number when written in Romans.

When the clearance between the column and beam end is sufficiently narrow, the heat flux from the clearance into the beam's X direction is minimal. In that case, the temperature gradient of the steel plate in the X direction is assumed to be sufficiently small. As a result, the temperature difference that occurs among dowels located in the same horizontal row is considered to be negligible. Thus, the transition of the rotation centre in the X direction can be ignored, which means $e_X^t \approx 0$. The methodology adopted to determine e_Y^t at each time step is presented in detail in Sect. 3.6. The current slip angle of dowel m to the grain, α_m^t, is:

$$\alpha_m^t = \begin{cases} \dfrac{\pi}{2} - \tan^{-1}\left(\dfrac{r_{Y,m}^t}{r_{X,m}^t}\right) & \left(r_{X,m}^t > 0\right) \\[2mm] \dfrac{3}{2}\pi - \tan^{-1}\left(\dfrac{r_{Y,m}^t}{r_{X,m}^t}\right) & \left(r_{X,m}^t < 0\right) \\[2mm] 0 & \left(r_{X,m}^t = 0 \text{ and } r_{Y,m}^t > 0\right) \\[2mm] \pi & \left(r_{X,m}^t = 0 \text{ and } r_{Y,m}^t < 0\right) \end{cases} . \tag{19}$$

Representing load–displacement responses of joineries with springs is the typical mechanical modelling method utilized in the component method [5, 6]. In the component method, it is generally assumed that bolts are short enough that their deformations can be ignored, allowing loads to be expressed as a simple function of displacement. However, unlike bolts used in steel structures, dowels used in
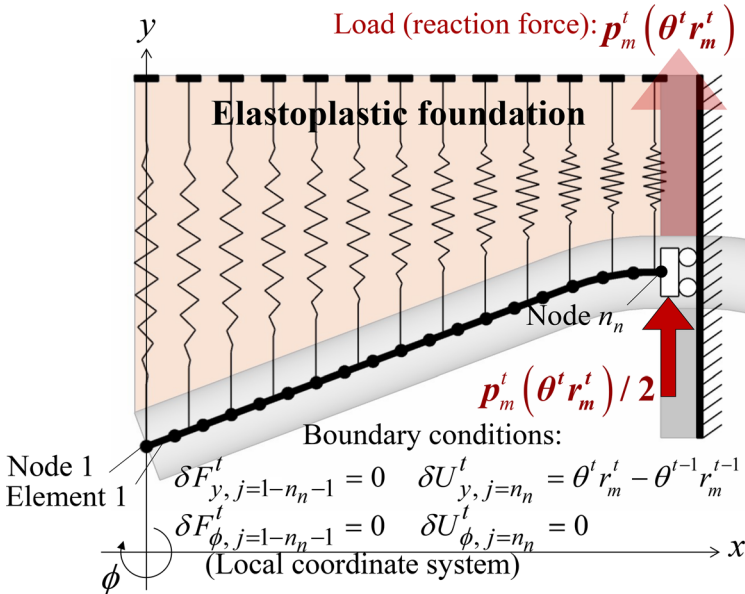

Figure 6. Model of a dowel on an elastoplastic foundation.

timber structures tend to be relatively slenderer and the underlying timber is considerably softer than steel. This implies that dowel deformation should not be ignored when determining its load–displacement (load–slip) response. Thus, in Eq. (16), the non-linear load–slip relationships for each dowel, $p_m^t(\theta^t r_m^t)$, are unknown functions of dowel deformation. To obtain $p_m^t(\theta^t r_m^t)$ accounting for the thermo-mechanical dowel deformation, the non-linear $M - \theta$ model divides dowels into a series of elements on an elastoplastic foundation, utilizing the BOEF theory and direct stiffness method in a time-incremental procedure as shown in Fig. 6. The governing equation of dowel deflection (Eq. 10) suggests that the deformation of the dowel depends on the embedding stiffness and the bending stiffness of the dowel, given that the dowel diameter remains constant during heating, assuming that the effect of thermal expansion can be ignored. Thus, by updating these two element properties of the elements at each time step, the simulation of load–slip relationships can consider the time history of temperature distribution and elastoplastic deformation.

3.2. Stress–Displacement Relationship of Elastoplastic Foundation

In non-linear $M - \theta$ model, timber is modelled as elastoplastic foundation. Using Foschi's approach [15], the relationship between embedding stress and element displacement, shown in Figs. 7 and 8, was assumed to take the exponential form:

$$\sigma_{\alpha=0}\left(T_i^t, v_{X,i}^t\right) = \left(K_{fh}\left(T_i^t\right)f_{h,\alpha=0} + k_{u,\alpha=0} \cdot v_{X,i}^t\right)\left[1 - \exp\left(\frac{-K_k\left(T_i^t\right)k_{s,\alpha=0}}{K_{fh}\left(T_i^t\right)f_{h,\alpha=0}}v_{X,i}^t\right)\right]$$
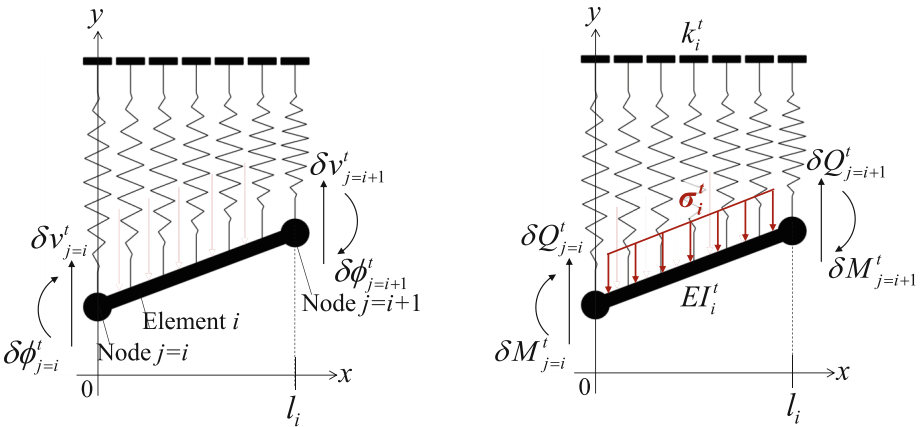
$$(20)$$

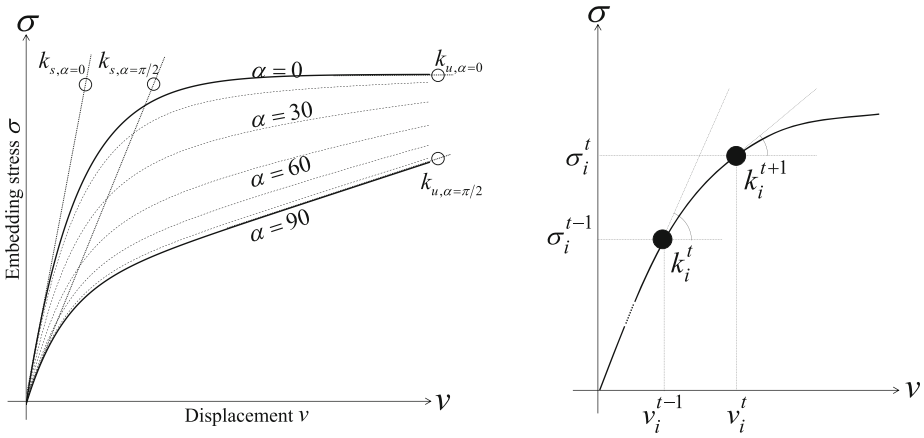
Figure 7. **Element on an elastoplastic foundation.**

Figure 8. Stress-displacement relationship of an elastoplastic foundation.

$$\sigma_{\alpha=\pi/2}\left(T_i^t, v_{Y,i}^t\right) = \left(K_{fh}\left(T_i^t\right)f_{h,\alpha=\pi/2} + k_{u,\alpha=\pi/2} \cdot v_{Y,i}^t\right)\left[1 - \exp\left(\frac{-K_k\left(T_i^t\right)k_{s,\alpha=\pi/2}}{K_{fh}\left(T_i^t\right)f_{h,\alpha=\pi/2}}v_{Y,i}^t\right)\right]$$

(21)

$$\sigma_{\alpha_m}\left(T_i^t, v_{\alpha_m,i}^t\right) = \frac{\sigma_{\alpha=0}\left(T_i^t, v_{X,i}^t\right) \cdot \sigma_{\alpha=\pi/2}\left(T_i^t, v_{Y,i}^t\right)}{\sigma_{\alpha=0}\left(T_i^t, v_{X,i}^t\right) \cdot \sin^2 \alpha + \sigma_{\alpha=\pi/2}\left(T_i^t, v_{Y,i}^t\right) \cdot \cos^2 \alpha}$$

(22)

where K_{fh} and K_k denotes the reduction factors for the embedding strength and stiffness, respectively, $f_{h,\alpha}$ denotes the embedding strength at the angle of α to the grain, $k_{s,\alpha}$ denotes the initial embedding stiffness at the angle of α to the grain, $k_{u,\alpha}$ denotes the secondary embedding stiffness at the angle of α to the grain, T denotes the element temperature, σ denotes the embedding stress applied to the element from the foundation, v denotes the element displacement, subscripts X and Y denote directions in the global coordinate system of the connection, $v_{X,i}^{t-1}$ denotes the element displacement of element i at time step $t-1$ in the direction of the X-axis, and $v_{Y,i}^{t-1}$ denotes the element displacement of element i at time step $t-1$ in the direction of the Y-axis. The current embedding stiffness for each element, $k_{\alpha_m,i}^t$ must be determined to calculate the deformation of the dowel at each time step. Using the element displacements from the previous time step, $t-1$, $k_{\alpha_m,i}^t$ can be updated by the following equations:

$$k_{\alpha=0,i}^t = \frac{\partial \sigma_{\alpha=0,i}^{t-1}}{\partial v_{X,i}^{t-1}} = K_k(T_i^t) \cdot k_{u,\alpha=0}$$

$$+ \left(K_k(T_i^t) \cdot k_{s,\alpha=0} - K_k(T_i^t) \cdot k_{u,\alpha=0} + \frac{K_k^2(T_i^t) \cdot k_{s,\alpha=0} \cdot k_{u,\alpha=0}}{K_{fh}(T_i^t) \cdot f_{h,\alpha=0}} v_{X,i}^{t-1} \right) \tag{23}$$

$$\times \exp\left(\frac{-K_k(T_i^t) \cdot k_{s,\alpha=0}}{K_{fh}(T_i^t) \cdot f_{h,\alpha=0}} \cdot v_{X,i}^{t-1} \right)$$

$$k_{\alpha=\pi/2,i}^t = \frac{\partial \sigma_{\alpha=\pi/2,i}^{t-1}}{\partial v_{Y,i}^{t-1}} = K_k(T_i^t) \cdot k_{u,\alpha=\pi/2}$$

$$+ \left(K_k(T_i^t) \cdot k_{s,\alpha=\pi/2} - K_k(T_i^t) \cdot k_{u,\alpha=\pi/2} + \frac{K_k^2(T_i^t) \cdot k_{s,\alpha=\pi/2} \cdot k_{u,\alpha=\pi/2}}{K_{fh}(T_i^t) \cdot f_{h,\alpha=\pi/2}} v_{Y,i}^{t-1} \right)$$

$$\times \exp\left(\frac{-K_k(T_i^t) \cdot k_{s,\alpha=\pi/2}}{K_{fh}(T_i^t) \cdot f_{h,\alpha=\pi/2}} \cdot v_{Y,i}^{t-1} \right)$$

$$\tag{24}$$

$$k_{\alpha_m,i}^t = \frac{k_{\alpha=0,i}^t \cdot k_{\alpha=\pi/2,i}^t}{k_{\alpha=0,i}^t \cdot \sin^2 \alpha_m^t + k_{\alpha=\pi/2,i}^t \cdot \cos^2 \alpha_m^t} \tag{25}$$

The X-axis and Y-axis of the global coordinate system corresponds to the direction parallel to the grain direction ($\alpha = 0$) and perpendicular to the grain ($\alpha = \pi/2$), respectively. The element displacements $v_{X,i}^{t-1}$ and $v_{Y,i}^{t-1}$ are calculated as the average of the adjacent nodal displacements, which are:

$$v_{X,i}^{t-1} = \frac{v_{X,j=i}^{t-1} + v_{X,j=i+1}^{t-1}}{2} \tag{26}$$

$$v_{Y,i}^{t-1} = \frac{v_{Y,j=i}^{t-1} + v_{Y,j=i+1}^{t-1}}{2} \tag{27}$$

The derivation of the current nodal displacements $v_{\alpha_m,i}^t$, $v_{X,j}^{t-1}$ and $v_{Y,j}^{t-1}$ is outlined in Sect. 3.4.

3.3. Stress–Strain Relationship of Steel

Figures 9 and 10 show the stress–strain relationship of the steel of dowels, which was assumed to have a bilinear form. The bending stiffness for each element can be updated using the following equation, assuming that the plane sections remain planar, namely:
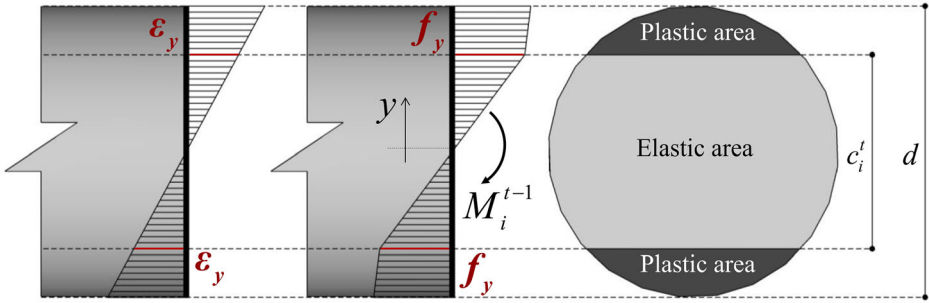
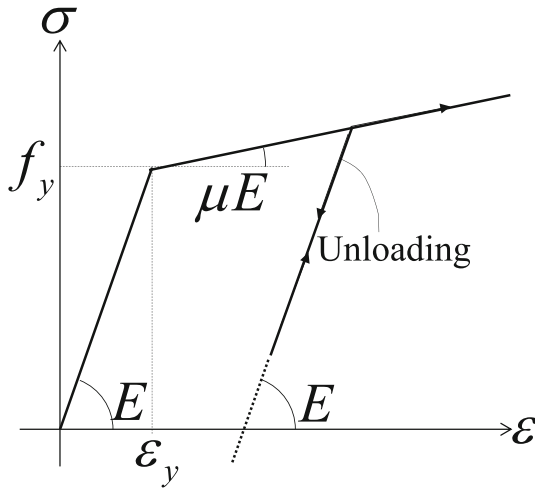**Figure 9. Stress and strain distribution of a plasticized element.**

Figure 10. Stress–strain relationship of steel.

$$EI_i^t = K_E(T_i^t)E\left[I\mu + I_{e,i}^t(1-\mu)\right] \tag{28}$$

where K_E denotes the reduction factor for the modulus of elasticity of steel, E denotes the modulus of elasticity of steel, I denotes the moment of inertia of the dowel $(d^4\pi/64)$, μ is the ratio of the modulus of elasticity to the modulus of plasticity, and $I_{e,i}^t$ denotes the moment of inertia of the element i's elastic cross-section. The derivation of Eq. (28) is included in Sect. 3.4. $I_{e,i}^t$ can be determined by the following integration:

$$I_{e,i}^t = \int_{-c_i^t/2}^{c_i^t/2} \int_{-\sqrt{d^4/4-y^2}}^{\sqrt{d^4/4-y^2}} y^2 \, dz \, dy$$

$$= \begin{cases} I & \text{Case I}: (M_{\max,i}^t \le M_i^{t-1} < M_y) \\ \frac{I}{\pi}\left(2\xi_i^t - \frac{\sin 4\xi_i^t}{4}\right) & \text{Case II}: (M_y \le M_{\max,i}^t \le M_i^{t-1}) \\ I & \text{Case III}: (M_i^{t-1} < M_{\max,i}^t) \end{cases} \tag{29}$$

where c_i^t denotes the height of the elastic cross-section of element i (see Fig. 9), ξ_i^t denotes $\arcsin(c_i^t/d)$, $M_{\max,i}^t$ denotes the maximum bending moment that element i has experienced before time step t, M_i^{t-1} denotes the bending moment of element i at the previous time step, and M_y denotes the yield bending moment. If the bending moment of element i, M_i^{t-1}, is lower than M_y or $M_{\max,i}^t$, the height of the elastic cross-section c_i^t is equal the dowel diameter d as the entire cross-section remains elastic; thus, $I_{e,i}^t$ corresponds to I. Figure 11 shows the schematic diagram of the condition branch in Eq. (29). The parameter ξ_i^t in Case II is a function of the bending moment of element i at the previous time step, $t-1$, given below:

$$|M_i^{t-1}| = \int \sigma y \cdot dA = 2K_{fy}(T_i^t) \cdot f_y \left[\frac{\mu I + \frac{I}{\pi}(1-\mu)\left(2\xi_i^t - \frac{\sin 4\xi_i^t}{2}\right)}{d \sin \xi_i^t} + \frac{d^3}{16}(1-\mu)\left(\cos \xi_i^t + \frac{\cos 3\xi_i^t}{3}\right) \right] \tag{30}$$

where K_{fy} is the reduction factor for yield stress of steel, and f_y is the yield stress of steel. Because ξ_i^t cannot be transformed into an explicit function of M_i^{t-1}, ξ_i^t is determined using the bisection method within the interval $\xi_i^t = [0, \pi/2]$. The previous bending moment of element i, M_i^{t-1}, is calculated as the average of the adjacent nodal bending moment, which is:

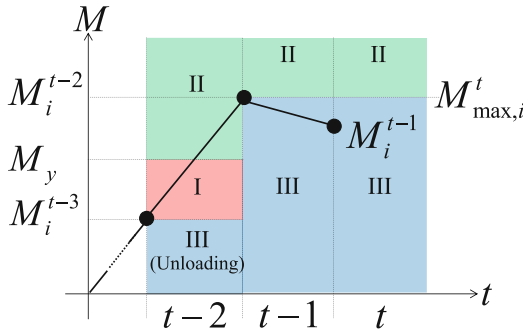$$M_i^{t-1} = \frac{M_{j=i}^{t-1} + M_{j=i+1}^{t-1}}{2} \tag{31}$$

Figure 11. Condition branch for updating bending stiffness.

The derivation of the nodal bending moment M_j^{t-1} is outlined in Sect. 3.4.

3.4. Element Stiffness Matrix Based on BOEF Theory

The main objective of this section is to derive the element stiffness matrix using the BOEF theory. The element stiffness matrix includes embedding stiffness and bending stiffness, which are updated at each time step using Eqs. (20) through (31). The current bending moment distribution along element i, $M_i^t(x)$, can be expressed using the current deflection curve of the element, $y_i^t(x)$, that is:

$$M_i^t(x) = \int \sigma y \cdot dA = - \left\{ \begin{array}{l} \int_{-c_i^t/2}^{c_i^t/2} \int_{-\sqrt{d^4/4-y^2}}^{\sqrt{d^4/4-y^2}} \left(K_E(T_i^t)E\frac{d^2y_i^t(x)}{dx^2}y^2 \right)dzdy \\ + \int_{c_i^t/2}^{d/2} \int_{-\sqrt{d^4/4-y^2}}^{\sqrt{d^4/4-y^2}} \left[\mu K_E(T_i^t)E\frac{d^2y_i^t(x)}{dx^2}y^2 + (K_{fy}(T_i^t)f_y - \mu K_E(T_i^t)E\varepsilon_y)y \right]dzdy \\ + \int_{-d/2}^{-c_i^t/2} \int_{-\sqrt{d^4/4-y^2}}^{\sqrt{d^4/4-y^2}} \left[\mu K_E(T_i^t)E\frac{d^2y_i^t(x)}{dx^2}y^2 - (K_{fy}(T_i^t)f_y - \mu K_E(T_i^t)E\varepsilon_y)y \right]dzdy \end{array} \right\}$$

$$\therefore M_i^t(x) = -K_E(T_i^t)E\left[\mu I + (1-\mu)I_{e,i}^t \right]\frac{d^2y_i^t(x)}{dx^2} - \frac{d^3}{8}\left(K_{fy}(T_i^t)f_y - \mu K_E(T_i^t)E\varepsilon_y \right)\left(\cos\xi_i^t + \frac{\cos 3\xi_i^t}{3} \right) \tag{32}$$

where f_y denotes the yield strength of steel, and K_{fy} denotes the reduction factor for the yield strength. Assuming that the element is sufficiently short, the distribution of ξ_i^t as well as $I_{e,i}^t$ along the element can be ignored. Thus, substituting Eq. (32) into Eq. (5) gives:

$$K_E(T_i^t)E\left[\mu I + (1-\mu)I_{e,i}^t \right]\frac{d^4y_i^t(x)}{dx^4} = q_i^t(x) \tag{33}$$

The current distributed load applied to the element from the elastoplastic foundation, $q_i^t(x)$, is assumed to be proportional to the deflection within time step t. Thus, the deflection curve of the element $y_i^t(x)$ satisfies the differential equation:

$$K_E(T_i^t)E\left[\mu I + (1-\mu)I_{e,i}^t \right]\frac{d^4y_i^t(x)}{dx^4} + k_{\alpha_m,i}^t d \cdot y_i^t(x) = 0 \tag{34}$$

Using Eq. (28), Eq. (34) can be written as:

$$EI_i^t\frac{d^4y_i^t(x)}{dx^4} + k_{\alpha_m,i}^t d \cdot y_i^t(x) = 0 \tag{35}$$

Because the differential Eq. (35) coincides with Eq. (7), the general solution of Eq. (35) has the same form as Eq. (10), that is:

$$y_i^t(x) = e^{\lambda_{\alpha_m,i}^t \cdot x}\left[A\cos\left(\lambda_{\alpha_m,i}^t \cdot x\right) + B\sin\left(\lambda_{\alpha_m,i}^t \cdot x\right)\right]$$
$$+ e^{-\lambda_{\alpha_m,i}^t \cdot x}\left[C\cos\left(\lambda_{\alpha_m,i}^t \cdot x\right) + D\sin\left(\lambda_{\alpha_m,i}^t \cdot x\right)\right] \qquad (36)$$

where A, B, C, and D are constants of integration, and $\lambda_{\alpha_m,i}^t$ stands for $\sqrt[4]{k_{\alpha_m,i}^t d / 4EI_i^t}$. As shown in Fig. 6, the boundary conditions of element i are as follows:

$$y_i^t(0) = \delta v_{j=i}^t, \ \dot{y}_i^t(0) = -\delta\phi_{j=i}^t, \ \ddot{y}_i^t(0) = \delta M_{j=i}^t/EI_i^t, \text{ and } \dddot{y}_i^t(0) = \delta Q_{j=i}^t/EI_i^t$$

$$(37)$$

where $\delta v_{j=i}^t$, $\delta\phi_{j=i}^t$, $\delta M_{j=i}^t$, and $\delta Q_{j=i}^t$ denote the incremental displacement, rotation, bending moment, and shear force of the left element end, respectively. The node number of the left element end coincides with the element number itself as the elements are arranged in a horizontal line. By substituting Eq. (37) into Eq. (36), the deflection curve for each element can be expressed using the following integration constants:

$$A = \frac{\delta v_{j=i}^t}{2} - \frac{\delta\phi_{j=i}^t}{4\lambda_{\alpha_m,i}^t} - \frac{\delta Q_{j=i}^t}{8EI_i^t \lambda_{\alpha_m,i}^t{}^3},$$
$$B = -\frac{\delta\phi_{j=i}^t}{4\lambda_{\alpha_m,i}^t} + \frac{\delta M_{j=i}^t}{4EI_i^t \lambda_{\alpha_m,i}^t{}^2} + \frac{\delta Q_{j=i}^t}{8EI_i^t \lambda_{\alpha_m,i}^t{}^3},$$

$$C = \frac{\delta v_{j=i}^t}{2} + \frac{\delta\phi_{j=i}^t}{4\lambda_{\alpha_m,i}^t} + \frac{\delta Q_{j=i}^t}{8EI_i^t \lambda_{\alpha_m,i}^t{}^3}$$

and

$$D = -\frac{\delta\phi_{j=i}^t}{4\lambda_{\alpha_m,i}^t} - \frac{\delta M_{j=i}^t}{4EI_i^t \lambda_{\alpha_m,i}^t{}^2} + \frac{\delta Q_{j=i}^t}{8EI_i^t \lambda_{\alpha_m,i}^t{}^3} \qquad (38)$$

With the values of all constants of integration, the incremental deflection of any point of the element can be calculated using Eq. (36). The incremental deformations and forces at the opposite element end, that is $x = l_i$, can be expressed using $\delta v_{j=i}^t$, $\delta\phi_{j=i}^t$, $\delta Q_{j=i}^t$, and $\delta M_{j=i}^t$ by recalling:

$$y_i^t(l_i) = \delta v_{j=i+1}^t, \ \dot{y}_i^t(l_i) = -\delta\phi_{j=i+1}^t, \ \ddot{y}_i^t(l_i) = -\delta M_{j=i+1}^t/EI_i^t, \text{ and } \dddot{y}_i^t(l_i)$$
$$= -\delta Q_{j=i+1}^t/EI_i^t \qquad (39)$$

The incremental element end forces can then be expressed using the incremental element end deformations. The element stiffness matrix is now expressed as:

$$
\begin{bmatrix}
\delta Q_{j=i}^t \\
\delta M_{j=i}^t \\
\delta Q_{j=i+1}^t \\
\delta M_{j=i+1}^t
\end{bmatrix}
=
$$

$$
\frac{2EI_i^t}{sh^2-s^2}
\begin{bmatrix}
2\lambda_{\alpha_m,i}^{t\,3}(sh\cdot ch+s\cdot c) & -\lambda_{\alpha_m,i}^{t\,2}(sh^2+s^2) & -2\lambda_{\alpha_m,i}^{t\,3}(sh\cdot c+ch\cdot s) & -2\lambda_{\alpha_m,i}^{t\,2}sh\cdot s \\
 & \lambda_{\alpha_m,i}^{t}(sh\cdot ch-s\cdot c) & 2\lambda_{\alpha_m,i}^{t\,2}sh\cdot s & -\lambda_{\alpha_m,i}^{t}(sh\cdot c-ch\cdot s) \\
 & & 2\lambda_{\alpha_m,i}^{t\,3}(sh\cdot ch+s\cdot c) & \lambda_{\alpha_m,i}^{t\,2}(sh^2+s^2) \\
\text{Sym.} & & & \lambda_{\alpha_m,i}^{t}(sh\cdot ch-s\cdot c)
\end{bmatrix}
\begin{bmatrix}
\delta v_{j=i}^t \\
\delta \phi_{j=i}^t \\
\delta v_{j=i+1}^t \\
\delta \phi_{j=i+1}^t
\end{bmatrix}
\tag{40}
$$

where $sh = \sinh(\lambda_{\alpha_m,i}^t\, l_i)$, $s = \sin(\lambda_{\alpha_m,i}^t\, l_i)$, $ch = \cosh(\lambda_{\alpha_m,i}^t\, l_i)$, and $c = \cos(\lambda_{\alpha_m,i}^t\, l_i)$. Once the current embedding stiffness and bending stiffness of all elements are obtained using Eqs. (20) through (31), the current element stiffness matrices are assembled into the current global stiffness matrix of the dowel such that the system can be expressed as:

$$
\delta \mathbf{F}^t = \mathbf{K}^t \cdot \delta \mathbf{P}^t \tag{41}
$$

where $\mathbf{K}^t$ denotes the current global stiffness matrix, $\delta \mathbf{F}^t$ denotes the current incremental nodal force vector, and $\delta \mathbf{U}^t$ denotes the current incremental nodal displacement vector. Inserting the known values, shown in Fig. 6, into Eq. (41) leads to:

$$
\begin{bmatrix}
\delta F_{y,j=1}^t = 0 \\
\delta F_{\phi,j=1}^t = 0 \\
\vdots \\
\delta F_{y,j=n_n-1}^t = 0 \\
\delta F_{\phi,j=n_n-1}^t = 0 \\
\delta F_{y,j=n_n}^t \\
\delta F_{\phi,j=n_n}^t
\end{bmatrix}
= \mathbf{K}^t
$$

$$
\cdot
\begin{bmatrix}
\delta U_{y,j=1}^t \\
\delta U_{\phi,j=1}^t \\
\vdots \\
\delta U_{y,j=n_n-1}^t \\
\delta U_{\phi,j=n_n-1}^t \\
\delta U_{y,j=n_n}^t = \theta^t r_m^t - \theta^{t-1} r_m^{t-1} (= \text{current slip increment}) \\
\delta U_{\phi,j=n_n}^t = 0
\end{bmatrix}
\tag{42}
$$

where the subscripts y and ϕ denotes directions in the local coordinate system of the dowel (Fig. 6) and n_n denotes the total number of nodes. Now, Eq. (42) is solvable, and the unknown nodal deformations and forces can be calculated. The

current nodal displacement in the global coordinate system can then be determined by the following summations:

$$v_{X,j}^t = v_{X,j}^{t-1} + \delta v_j^t \cdot \cos \alpha_m = v_{X,j}^{t-1} + \delta U_{y,j}^t \cdot \cos \alpha_m \qquad (43)$$

$$v_{Y,j}^t = v_{Y,j}^{t-1} - \delta v_j^t \cdot \sin \alpha_m = v_{Y,j}^{t-1} - \delta U_{y,j}^t \cdot \sin \alpha_m, \qquad (44)$$

$$v_{\alpha_m,j}^t = \sqrt{v_{X,j}^t{}^2 + v_{Y,j}^t{}^2} \qquad (45)$$

3.5. Element End Force and Reaction Force

Once all the current element end displacements are obtained, in Eq. (45), the current element end forces can be calculated by equilibrium with the σ calculated from Eq. (22). As shown in Fig. 12, the current shearing forces and bending moments can be calculated by the following integrations:

$$Q_j^t = \sum_{i=1}^{j-1} \sigma_{\alpha_m}\left(T_i^t, v_{\alpha_m,i}^t\right) \cdot l_i \cdot d \qquad (46)$$

$$M_j^t = \sum_{i=1}^{j-1} \left[\sigma_{\alpha_m}\left(T_i^t, v_{\alpha_m,i}^t\right) \cdot l_i \cdot d \cdot \left(\frac{l_i}{2} + l_{i+1} + l_{i+2} + \cdots + l_{j-1}\right)\right] \qquad (47)$$

The node $j = n_n$ is the contact point with the steel plate. Thus, the current reaction force for each dowel p_m^t is obtained using:

$$p_m^t\left(\theta^t r_m^t\right) = 2Q_{j=n_n,m}^t = 2\sum_{i=1}^{n_n-1} \sigma_{\alpha_m}\left(T_{i,m}^t, v_{\alpha_m,i}^t\right) \cdot l_{i,m} \cdot d \qquad (48)$$

3.6. Distance From Centroid Axis to the Neutral Axis

The axial force caused by the rotation around the neutral axis must be 0. Thus, the amount of $p_m^t\left(\theta^t r_m^t\right) \cos \alpha_m$ was checked against the permissible error:

$$\left|\sum_{m=1}^{n_d} p_m^t\left(\theta^t r_m^t\right) \cos \alpha_m\right| \leq \text{permissible error} \qquad (49)$$
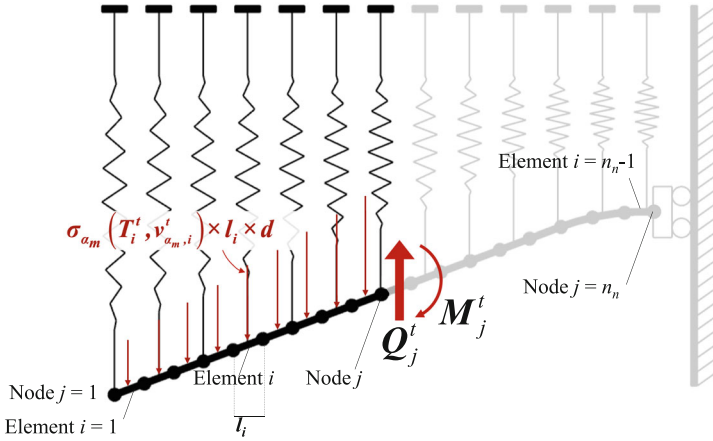
Figure 12. Equilibrium between element end forces and stress from an elastoplastic foundation.

If convergence was not obtained, the interval for the bisection method and the current Y-coordinate of the rotation centre from the centroid point, $e_Y^{t,c}$, were updated from the following condition branch:

$$
\left[e_{Y,\text{high}}^{t,c+1}, e_{Y,\text{low}}^{t,c+1}\right] =
\begin{cases}
\left[e_{Y,\text{high}}^{t,c}, e_Y^{t,c}\right] & \left(\sum_{m=1}^{n_d} p_m^t\left(\theta^t r_m^t\right)\cos\alpha_m^t > \text{permissible error}\right) \\
\left[e_Y^{t,c}, e_{Y,\text{low}}^{t,c}\right] & \left(\sum_{m=1}^{n_d} p_m^t\left(\theta^t r_m^t\right)\cos\alpha_m^t < -\text{permissible error}\right)
\end{cases}, e_Y^{t,c+1}
$$

$$
= \frac{e_{Y,\text{high}}^{t,c+1} + e_{Y,\text{low}}^{t,c+1}}{2}
$$

$$(50)$$

The initial values, $e_{Y,\text{high}}^{t,c=0}$ and $e_{Y,\text{low}}^{t,c=0}$, represent the distances from the centroid point to the uppermost and downmost dowels, respectively. After redetermining $r_{Y,m}^t$ from Eq. (18) using $e_Y^{t,c+1}$, the calculation is reduced from Eq. (18), with the current slip increment $\theta^t r_m^t - \theta^{t-1} r_m^{t-1}$ being recalculated.

3.7. Reduction Factor

The modulus of elasticity and yield strength of steel at elevated temperatures were reduced according to the reduction factors recommended in Eurocode 3 [34]. Meanwhile, the reduction factors for the embedding stiffness and strength of timber were determined from available experimental data [35], because there are no recommendations in Eurocode 5. The reduction factors are shown in Fig. 13. The test specimens consisted of Japanese larch of the same strength class as the frame specimens described later. Each specimen consisted of two glulam blocks con-
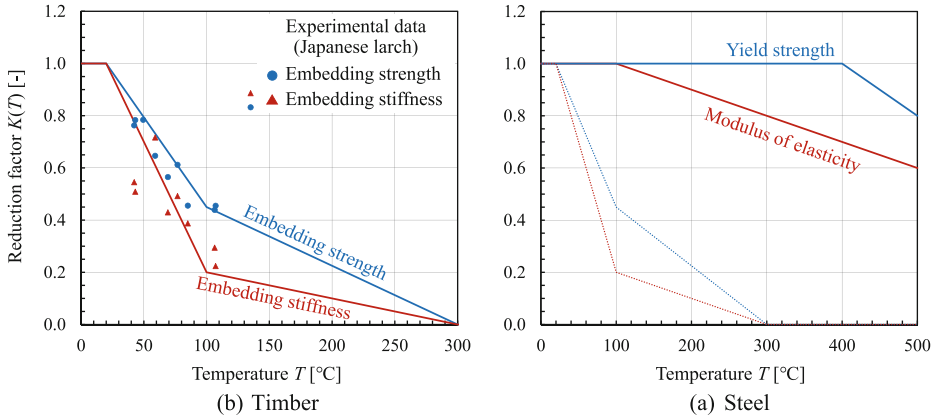
Figure 13. Reduction factor.

nected by a 9-mm-thick steel plate, with two 16-mm-diameter dowels penetrating the pre-drilled holes in the glulam blocks and steel plate. Please refer to Fig. 1 in the reference [35] for a more detailed configuration of the specimens. The experimental procedure [35] was as follows: first, the single-dowelled specimens (Japanese larch) were heated for 1–2 h in an electric furnace with an air temperature of 100, 150, or 200°C; subsequently, the specimens were removed from the furnace and covered with a heat-resistant glass cloth; and finally, the specimens were compressed to obtain the load-slip curve, embedding stiffness, and embedding strength. Each specimen was unloaded when the displacement surpassed 8 mm and embedding strength was obtained. The temperature of the specimen was measured using two thermocouples attached to the centre of the dowel. The maximum specimen temperature was nearly 100°C, which was recorded by the specimen heated at an air temperature of 200°C for two hours. The reduction factors above 100°C were linearly interpolated up to 300°C referencing the reduction factor for timber strength and elastic modulus recommended in Eurocode 5 [36].

The reduction factors were calculated based on the time history data of the element temperatures. They were then multiplied to the corresponding mechanical properties at each time step, as shown in Eqs. (20)–(31).

3.8. Load–Slip Relationships of Non-linear Springs at High Temperature

Figure 14 shows the analytical results, obtained using Eqs. (20)–(48), for the load–slip relationships of the specimens at high temperature [35]. The results agreed well with the available experimental results at 20, 60, and 100°C, which indicates that load–slip relationships of dowels at ambient and high temperatures were properly modelled in the non-linear $M - \theta$ model. Figure 15 shows the flow chart of the calculation procedure of the non-linear $M - \theta$ model. All calculation procedures were programmed in the programming language C + + .
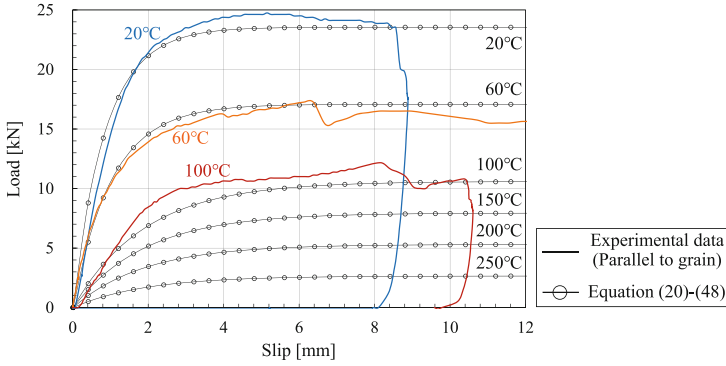
Figure 14. **Experimental and analytical results of load–slip relationships at high temperature.**
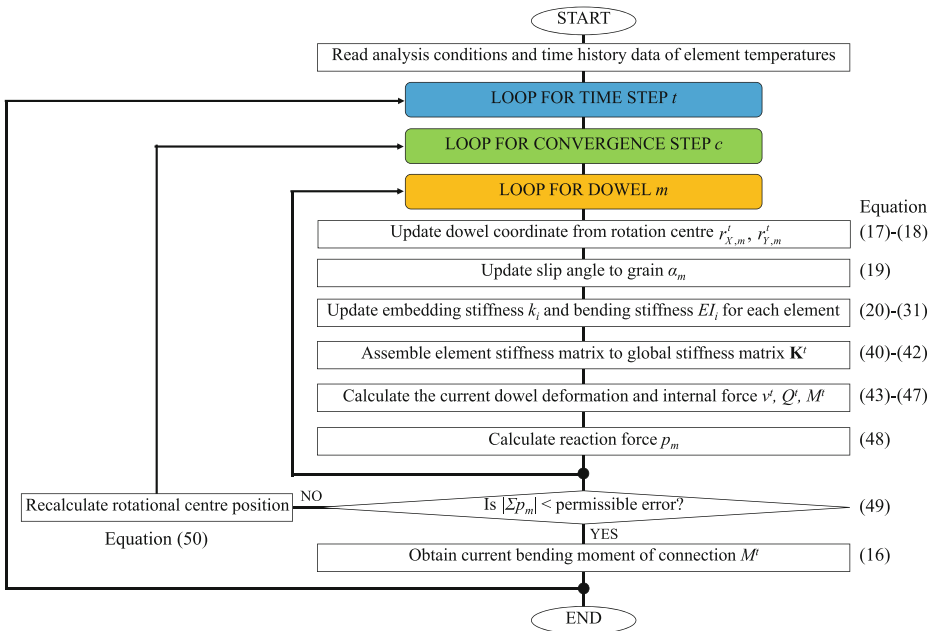

Figure 15. **Flow chart – Calculation procedure of the non-linear $M - \theta$ model.**

4. Experimental Program

4.1. Test Specimen

Two load-bearing tests were conducted on large-scale glulam frames under ambient and fire conditions. The detailed configuration of the specimens is shown in Figs. 16 and 17.
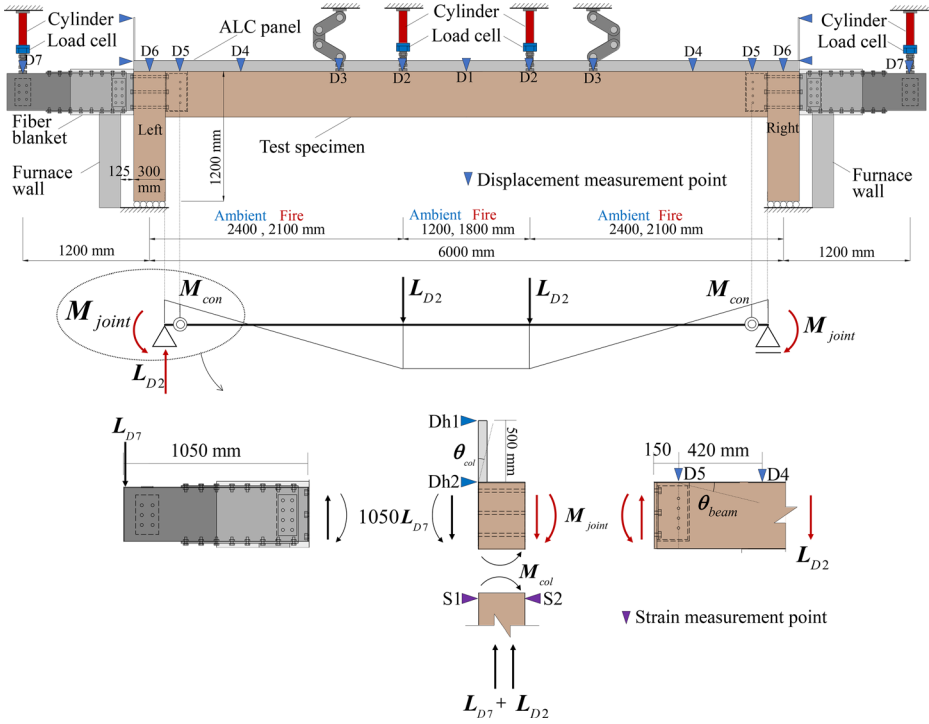
Figure 16.   Test setup.
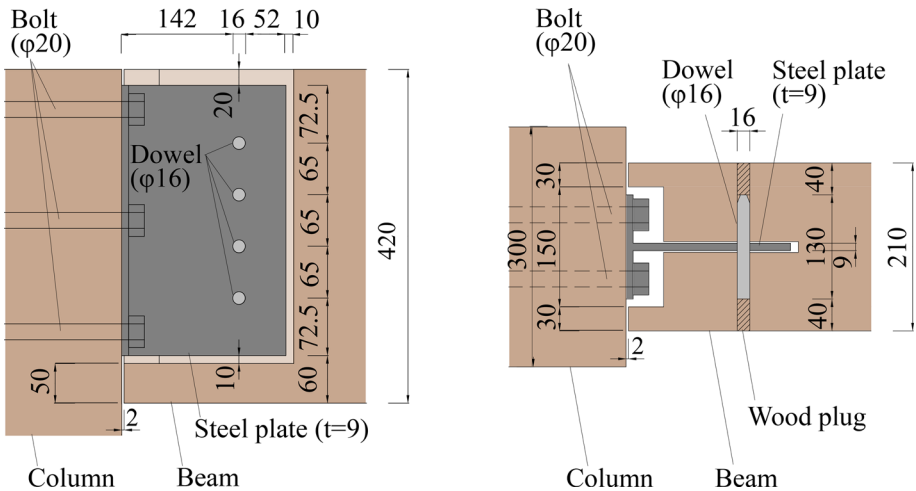
Figure 17.   Connection configuration of the specimen (unit: mm).

These specimens consisted of Japanese larch with an average density of 0.473 g/cm³. The cross-sectional dimensions of the column and beam were 300 mm × 300 mm and 420 mm × 210 mm, respectively. The column-beam connections were wood-steel-wood dowel-type connections consisting of four dowels and a T-stub slotted-in steel plate, manufactured with a 9-mm thick steel plate. The steel plate had four circular holes with a diameter of 17 mm, while the beam had four circular holes with a diameter of 16 mm. To connect the column to the glulam beam, the steel plate was affixed to the column using 20-mm-diameter bolts. A 1050-mm-long steel beam was connected to the opposite side of the column. The beam was lifted to insert the plate webs into 10.5-mm-wide cuts at the beam ends, as well as to employ 50-mm-deep timber layers that insulated both plate bottoms. Dowels with a diameter of 16 mm were then inserted through the holes to connect the plates and beam. The length of the dowels was 130 mm, which was 80 mm less than the width of the beam, allowing for the embedding of the dowel heads with 40-mm wood plugs that were used as fire protection for the heads. The width of the clearance between the column and beam end was less than 2 mm to minimize heat flux from the clearance to the beam end.

4.2. Instrumentation

Temperatures within the cross-section of the beam's midspan and both right-side and left-side connections were measured by eight type-K thermocouples. The holes prepared in the glulam beam to insert the thermocouples had the same diameter as those of the thermocouple cables. Additionally, these holes were drilled from the top of the beam and covered by ALC panels during the test to prevent heat penetration that could potentially influence the thermal measurements. Before inserting the dowels, additional holes were drilled on the surface of the circular holes, and the thermocouples were inserted to measure the connection temperature. Figure 18 shows the temperature measurement points of the right-side and left-side connections. Details regarding temperature measurement points, temperature measurement results, and related discussions have been previously reported by Kikuchi et al. [37]. In the present paper, only the results of temperature measurements at the connections, which are essential for discussing the experimental and analytical results, are presented.

Loads on the specimens were measured using load cells attached to points D2s and D7s. Displacements from D1 to D7s, as well as Dh1s and Dh2s, were measured with transducers installed at the displacement measurement points shown in Fig. 16. In the ambient test, strain gauges were attached to the strain measurement points S1 and S2 to measure the bending moment of the column. The strain gauges were only attached to the left column.

4.3. Test Set-Up and Procedure

The tests were conducted in the gas-fuelled furnace located at General Building Research Corporation of Japan (GBRC) in Ikeda, Osaka, Japan. In both ambient and fire tests, a specimen was put inside the furnace with the attached steel beams extending outside the furnace. The steel beams penetrated the relatively wide holes
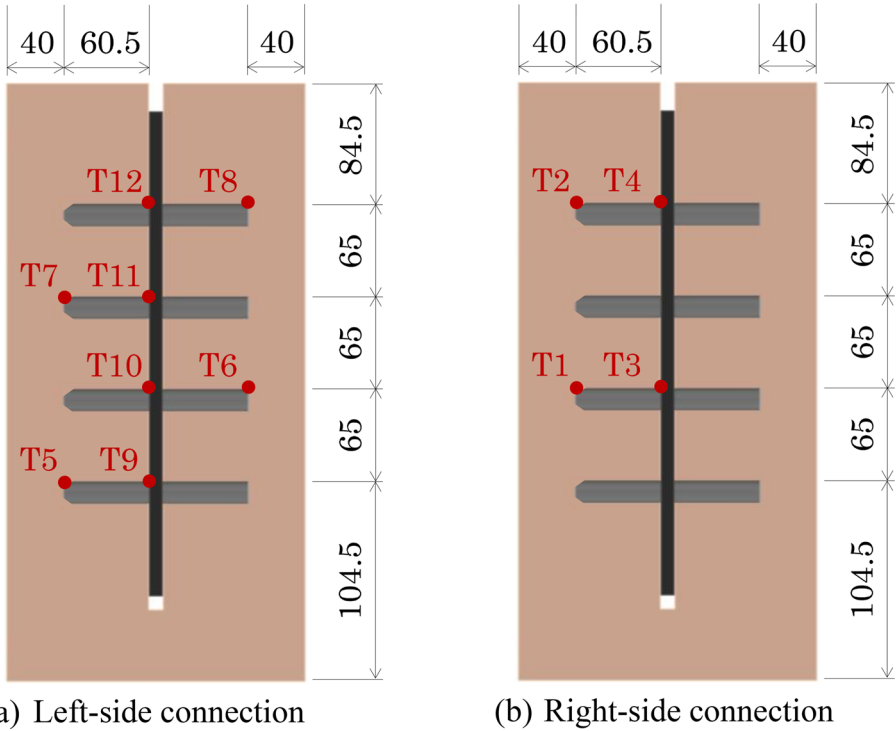
(a) Left-side connection (b) Right-side connection

Figure 18. Temperature measurement points (unit: mm).

in the furnace walls, and these holes were filled with soft fibre blankets. During the tests, the furnace walls did not support the steel beams due to minimal displacement of the steel beams at the furnace walls and ends. Figure 19 shows the specimen positioned in the furnace. To apply vertical loads to the specimen, two hydraulic cylinders were utilized at point D2s, mounted above the furnace on a robust steel loading frame. The hydraulic cylinders installed at points D7s were manually controlled to restrain the vertical displacements of the steel beam ends during the tests to ensure that the dowel-type connections exhibited rotational resistance.

In the ambient test, the load on point D2s was increased until failure was confirmed. The load on point D2s rapidly decreased after the tensile surface of the beam ruptured (see Figure 20). Therefore, the failure criterion for the frame was assumed to occur when the load on point D2s recorded the maximum load up until the point of rupture. In the fire test, the timber frame was exposed to the fire according to the ISO 834 standard temperature–time curve on all sides except the beam's top one, imitating the presence of a slab on top of the beam. ALC panels with slits at intervals of 750 mm were used to fire-protect the top of the timber beam and prevent the panels from reinforcing the bending stiffness of the beam. Before the heating commenced, the specimen was preloaded to 100% of the design bending moment (28.5 kN at point D2s), which was calculated using the reduced cross-section method recommended in the Japanese standard for 60-min

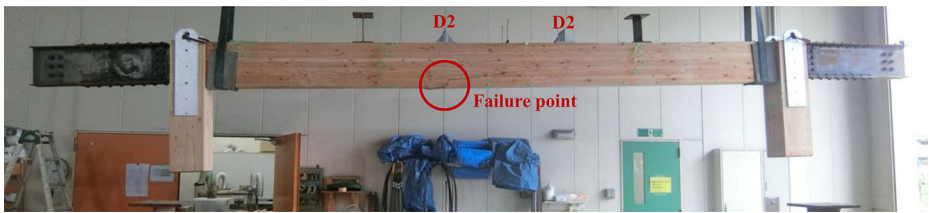**Figure 19. Specimen set in the furnace.**

Figure 20. Specimen after the ambient test.

fire-resistant timber structures [38]. According to the standard, the charring rate of 0.75 mm/min was assumed under fire conditions, and the dowel-type connections were assumed to be pinned connections. The assumed cross-section after 60 min of fire exposure consisted of a charred depth of 45 mm (0.75 mm/min × 60 min) on the three sides and the effective cross-section inside the charred layer. The failure criterion for the frame was assumed to occur when the load on point D2s decreased to 95% of the preload. In the ambient test, with a loading span of 1200 mm, no connection failures were observed. To obtain the strength of the connections in the fire test, the loading span was increased from 1200 to 1800 mm, thus intensifying the conditions on the connections by reducing the shear span.

4.4. Measurement of $M - \theta$ Relationships During Experiments

As shown in Fig. 16, the specimens can be modelled as a simply supported beam that is subject to bending moments from the beam-to-column joints, M_{joint}, and vertical loads on point D2s, L_{D2}. The experimental results of the $M - \theta$ relationships, compared to results of the linear and non-linear $M - \theta$ models in Chapter 6, represent the relationship between the bending moment at the dowel

location, M_{con}, and the relative rotation angle between the beam end and column head, θ_{con}:

$$M_{con} = 150L_{D2} - M_{joint} = 150L_{D2} - (1050L_{D7} + M_{col}) \tag{51}$$

$$\theta_{con} = \theta_{beam} - \theta_{col} \tag{52}$$

$$\theta_{beam} = \arcsin\left(\frac{D_4 - D_5}{420}\right) \tag{53}$$

$$\theta_{col} = \arcsin\left(\frac{D_{h1} - D_{h2}}{500}\right) \tag{54}$$

where L_{D7} denotes the measured load on point D7, M_{col} denotes the bending moment within the column, θ_{beam} denotes the rotation angle of the beam end, θ_{col} denotes the rotation angle of the column head, and D_4, D_5, D_{h1}, and D_{h2} are the displacements (mm) at the corresponding measurement points. In the ambient test, the strain gauges that were attached to the compressive (S2) and tensile (S1) surfaces recorded negative and positive strains, respectively, which means the columns resisted a bending force. Therefore, the bending moment of the columns must be considered when calculating the bending moment of the tested connections. The bending moment in an optimised roller-supported column must be zero; however, in the experiments, the surface of the column base could resist rotation owing to axial compression, which resulted in the pure bending of the column. In the ambient test, M_{col} was measured using:

$$M_{col} = Z \cdot E \frac{\varepsilon_{S1} - \varepsilon_{S2}}{2} \tag{55}$$

where Z is the section modulus of the columns (4.5×10^6 mm^3), E is the modulus of elasticity of the columns (9500 N/mm^2, [38]), and ε_{S1} and ε_{S2} are the strains at the corresponding measurement points.

5. Experimental Results

5.1. Load-Bearing Capacity and Fire Resistance Time of the Specimen

Figure 20 shows the specimen after the ambient test. Figure 21 shows the load–displacement relationship obtained in the test under ambient conditions. The vertical axis shows L_{D2} and L_{D7}, while the horizontal axis shows the displacement at the midspan of the beam (point D1). A finger joint on the beam bottom near point D2 fractured when L_{D2} reached the maximum value of 91.0 kN, leading to a loss of load-bearing capacity for the specimen. Semi-rigidity was exhibited in both connections, demonstrating comparability as minimal differences were observed
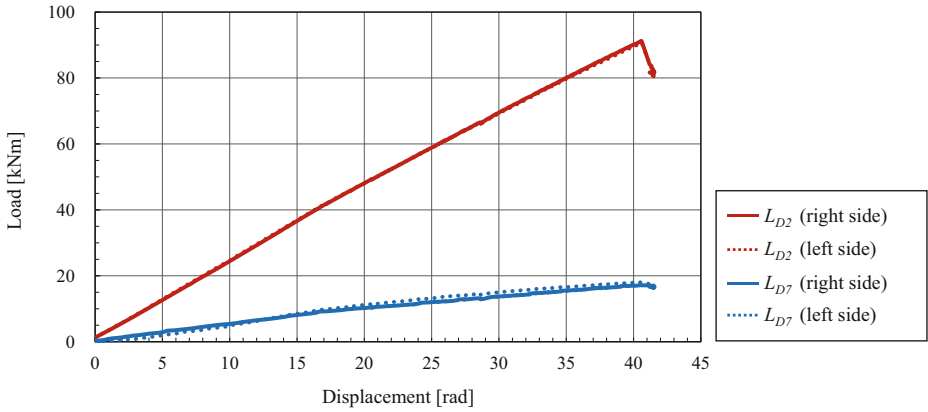
Figure 21. Load–displacement relationship in the ambient test.

Figure 22. Specimen after the fire test.

between left and right L_{D7}. Furthermore, these two loads exhibited proportionality to the increase in displacement of D1.

Figure 22 shows the specimen after the fire test. Figure 23 shows the time–displacement relationship obtained in the test under fire conditions. The vertical axis shows the displacement at the midspan of the beam (point D1), while the horizontal axis shows the heating time. The displacement is not zero at the beginning of heating because of displacement developed during the pre-loading phase before heating commenced. The specimen withstood 91 min of ISO standard fire, and the beam bottom near the point D2 failed in bending. Figure 24 shows the time transition of L_{D2} and L_{D7}. Left and right L_{D2} were successfully controlled to be constant throughout the test and sharply declined at 91 min when the specimen failed. While L_{D7} on the left side recorded a relatively small value, both left and right L_{D7} remained almost constant, with no observable difference in their behavior. The displacement restraint at the ends of the steel beams was effective, and the rotational resistance of the connections, in response to the displacement restraint, was exhibited.

5.2. Temperature of the Dowels in the Fire Test

Figure 25 shows the time–temperature relationship of the right-side connection. The temperatures of the dowel ends (points T1 and T2) continued to increase
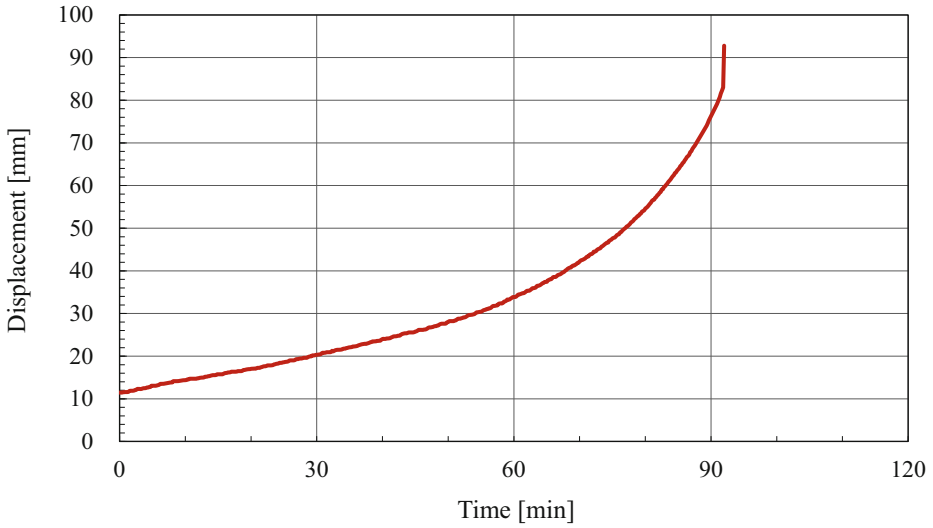
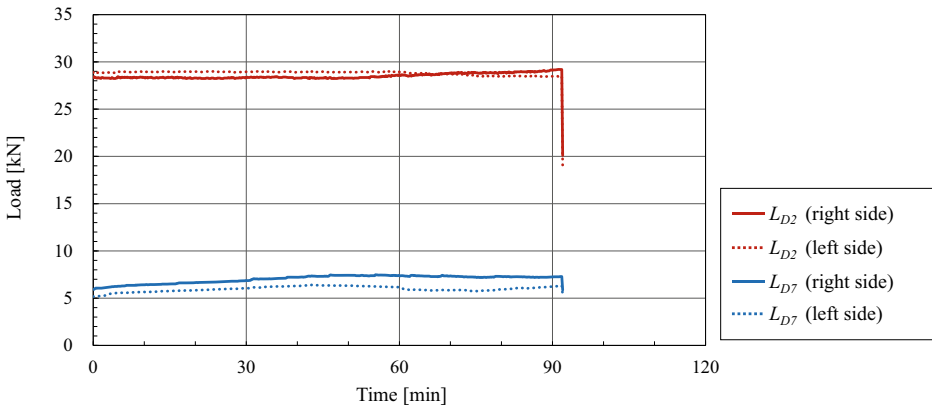**Figure 23. Time–displacement relationship in the fire test.**

Figure 24. Time transition of L_{D2} and L_{D7}.

after the beginning of heating, surpassing 100°C around 50 min. While the temperature of point T1 stagnated after 50 min due to water evaporation, both temperatures then resumed to increase and reached approximately 280°C at 91 min at the end of the experiment. The temperatures of the dowel centres (points T3 and T4) continued to increase after the beginning of heating, with the temperature at point T3 reaching 100°C around 67 min and the temperature at point T4 around 62 min. Neither of these temperatures reached the charring temperature of 300°C until the end of the experiment. The temperature at T4 was slightly higher than that at T3. This discrepancy may be attributed to heat influx from the clearance between the top of the beam end and the column into the steel plate resulting
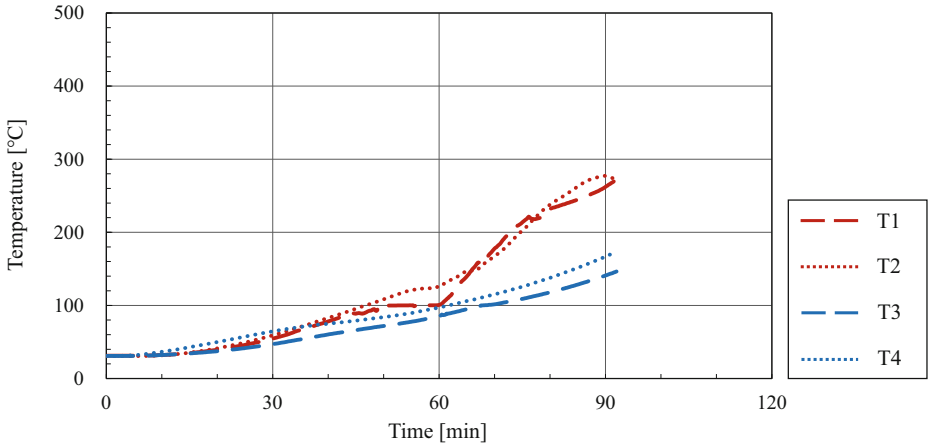
Figure 25. Time–temperature relationship of the right-side connection.
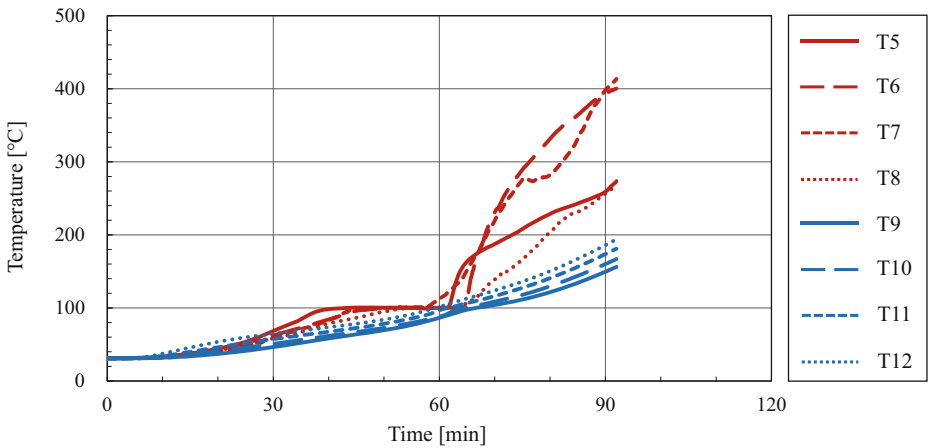
Figure 26. Time–temperature relationship of the left-side connection.

from the rotation of the connection. Nevertheless, given that the original clearance was very small (less than 2 mm), the temperature difference did not reach a significant level.

Figure 26 shows the time–temperature relationship of the left-side connection. The temperatures of the dowel ends (points T5, T6, T7, and T8) continued to increase after the beginning of heating, surpassing 100°C around 40 min. Although these temperatures stagnated after 40 min due to water evaporation, they resumed increasing after 60 min. The temperatures at T6 and T7 increased

more rapidly than those at T5 and T8, both reaching 400°C by the end of the experiment. However, the behaviour of the temperatures at T5 and T8 after 60 min closely resembled that of T1 and T2. The temperatures of the dowel centres (points T9, T10, T11, and T12) continued to increase after the beginning of heating. Due to the same factors influencing the temperature of the left-side connection, the temperature at T12 was consistently higher than that at T9 as well.

5.3. Deformation of the Dowels After the Tests

After both tests, the right-side connections were removed with a chainsaw, and the dowels were extracted from the cylinder-shaped holes. Figure 27a shows the dowels after the ambient test. Deformation remained in the dowels, especially in the top and bottom dowels, after the test. This deformation is because the top and bottom dowels were farthest from the rotation centre, experiencing a greater load as the connection resisted a bending moment. Figure 27b shows the dowels after the fire test, and no significant residual deformation was observed. This can be attributed to the slow decrease in the mechanical properties of steel compared to timber, as illustrated in Fig. 13b. Considering that all connection temperatures were below 400°C where the strength of the steel decrease (see Fig. 25), the embedding strength of the timber diminished gradually, while the steel retained its strength at ambient temperatures.

5.4. $M - \theta$ Relationship at Ambient Temperature

Figure 28 shows the experimental result of the $M - \theta$ relationship at ambient temperatures calculated using Eqs. (51)–(55). As the strain gauges were only attached

(a) The ambient test   (b) The fire test

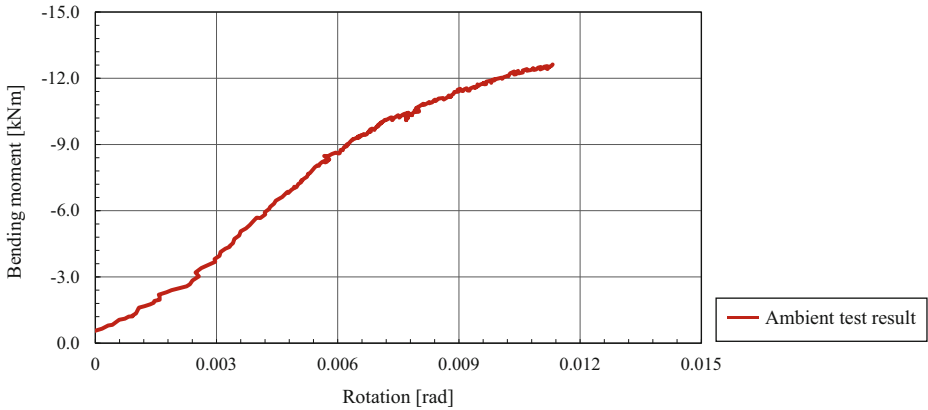**Figure 27.   Dowels after the tests.**

Figure 28. *M − θ* **relationship in the ambient test.**

to the left column, M_{col} in the ambient test was measurable only for the left-side column. Therefore, Fig. 28 shows the experimental result of the $M − θ$ relationship of the left-side connection. While the bending moment of the connection increased almost linearly before 0.003 rad, the rotational stiffness of the connection increased after 0.003 rad. Figure 29a shows the left-side connection when the load on D2 reached 22 kN. Since the beam end was in contact with the column, the increase in the rotational stiffness is attributed to the contact between the beam end and column. When the rotation angle of the connection exceeded 0.006 rad, the rotational stiffness decreased due to the yielding of the wood and the dowels.

5.5. $M − θ$ *Relationship at High Temperature*

M_{col} in the fire test could not be measured using strain gauges as they are not fire-proof and cannot be used under fire conditions. Therefore, the relationship between M_{col} and $θ_{col}$ in the ambient test, shown in Fig. 30, was applied to both columns to calculate M_{col} in the fire test. M_{con} under fire conditions were calculated by substituting M_{col} in the ambient test corresponding to $θ_{col}$ in the fire test into Eq. (51). It should be noted that this approach may lead to an overestimation of M_{col} in the fire test as the stiffness of the relationship between M_{col} and $θ_{col}$ depends on the bending stiffness of the column, which significantly decreases due to charring under fire conditions. Therefore, in Figs. 34 and 35, the solid line represents the $M − θ$ relationship using the relationship between M_{col} and $θ_{col}$ in the ambient test, while the dotted line represents the $M − θ$ relationship assuming M_{col} to be 0. The actual $M − θ$ relationship is expected to be close to the solid line in the early stages of the fire and close to the dotted line in the ultimate stages of the fire, as the bending stiffness of the columns decreases due to charring. The time transitions of $θ_{beam}$ and $θ_{col}$ in the fire test is shown in Figs. 31 and 32, respectively. $θ_{beam}$ was calculated using Eq. (53) and $θ_{col}$ was calculated using Eq. (54).
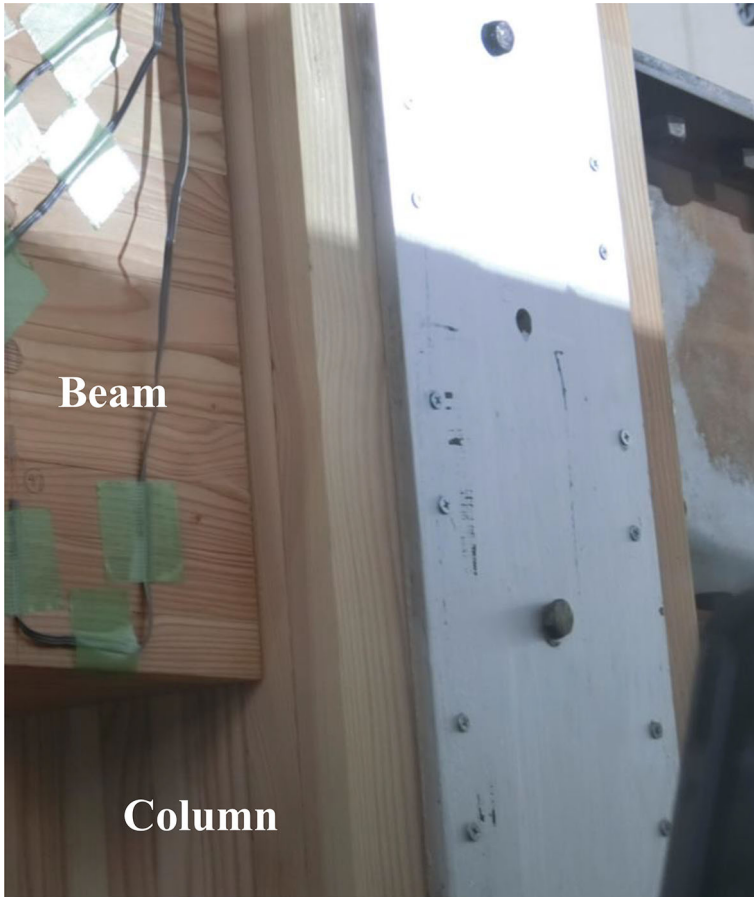
Figure 29.   Left-side connection when the load on D2 reached 22 kN.

Figure 33 shows θ_{con} calculated using Eq. (52). Little difference was observed between the time transitions of left and right θ_{con}.

Figure 34 shows the $M - \theta$ relationships of the right-side connection. In the pre-loading phase, the $M - \theta$ relationship increased almost linearly. After the beginning of heating, the bending moment increased with the increase in the connection rotation up to 50 min, while the rotational stiffness of the connection decreased with increasing temperature. At this point, the temperatures at points T1 and T2 exceeded 100°C. Subsequently, the connection sustained a constant bending moment because the increase in bending moment resulting from the increased rotation angle of the connection was approximately offset by the reduction in bending moment due to the decreased rotational stiffness. Considering the possibility that M_{col} was minimal at the end of the fire, the right-side connection could have resisted a bending moment of approximately 3 kNm at the end of the experiment. Figure 35 shows the $M - \theta$ relationships of the left-side connection.
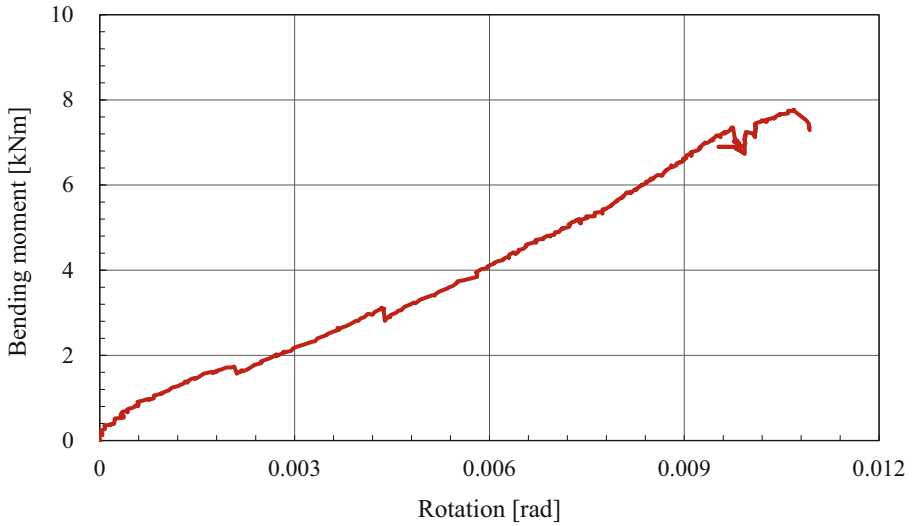
Figure 30. Relationship between M_{col} and θ_{col} in the ambient test.
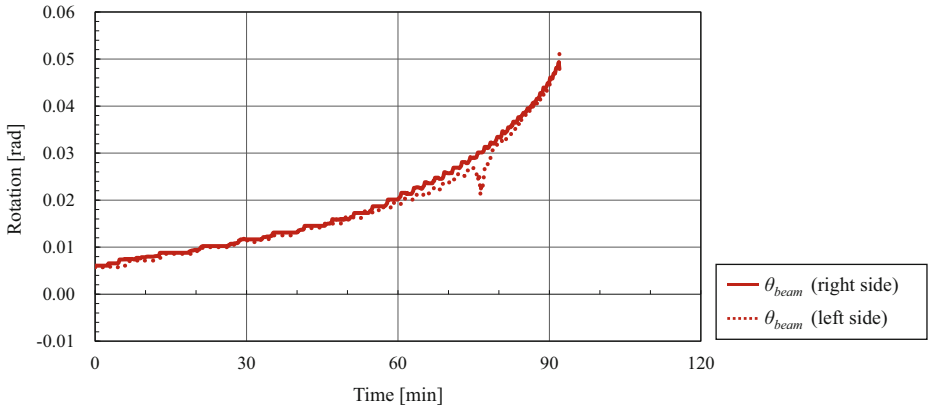

Figure 31. Time transition of θ_{beam}.

The bending moment of the left-side connection increased until 50 min. However, the bending moment started to decrease after 50 min and exhibited an unstable behaviour after 70 min, even though the displacement restraint at the steel beam end was sufficient. This can be attributed to the time transition of θ_{col}, as shown in Fig. 32. θ_{col} of the left-side column declined rapidly at 30 min, followed by a continuous decrease and an unstable behaviour after 70 min. The measurement of θ_{col} of the left-side column was considered inadequate, and the accurate $M - \theta$ relationship could not be calculated.
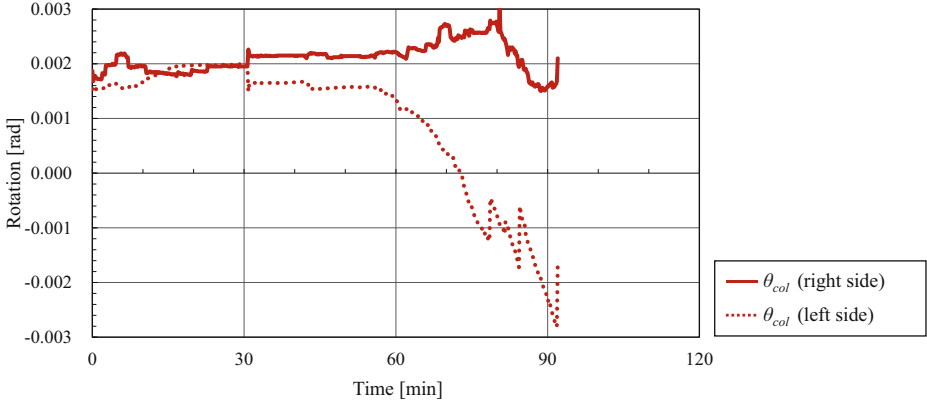
Figure 32.   Time transition of θ_{col}.

Figure 33.   Time transition of connection rotations (θ_{con}).

6. Model Validation

6.1. Model Validation at Ambient Temperature

Figure 36 compares the experimental result with the result calculated using the linear $M - \theta$ model (Eq. 1). The dotted line in Fig. 36 shows the $M - \theta$ relationship calculated using:

$$M = \sum_{m=1}^{n_d} \left(k_{\alpha_m} \cdot d \cdot l \cdot r_m^2 \right) \theta \tag{56}$$

Equation (56) assumes that dowels are rigid bodies, which in turn overestimated the experimental result. Since the linear $M - \theta$ model assumes the elasticity of dowels and timber, the calculated and experimental results agreed well up until
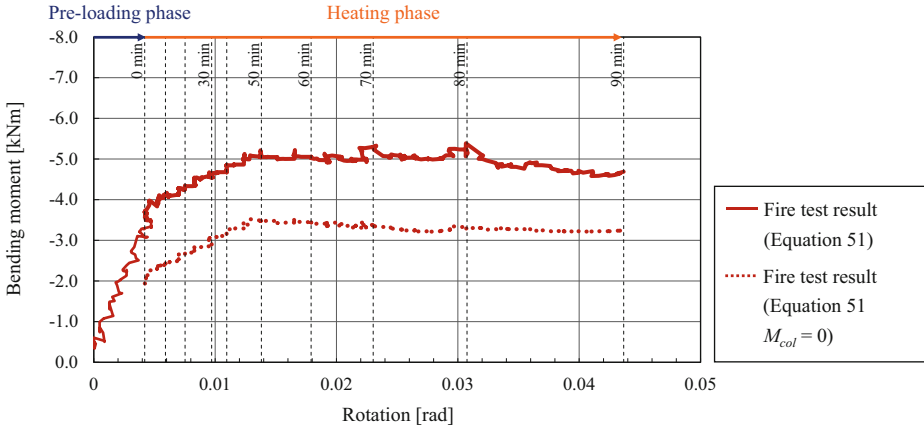
Figure 34. $M - \theta$ **relationship in the fire test (right-side connection).**
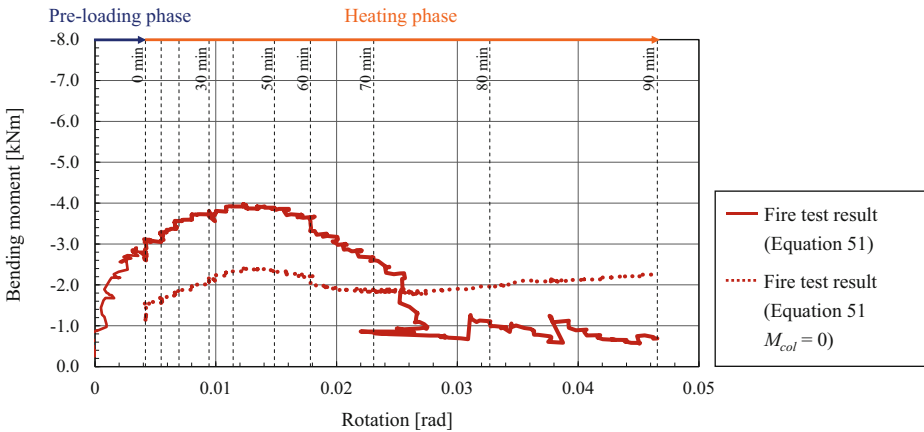

Figure 35. $M - \theta$ **relationship in the fire test (left-side connection).**

the rotation surpassed 0.003. However, at higher rotations, the calculated underestimated the experimental result, with a discrepancy of up to 25%. This discrepancy is due to an increase in the rotational stiffness of the specimen connection resulting from contact between the lower beam end and the column, a factor ignored in the linear $M - \theta$ model. When the rotation surpassed 0.006 rad, the rotational stiffness of the specimen connection began to decrease owing to yielding.

6.2. Model Validation at High Temperature

The time history data for element temperatures is necessary for the non-linear $M - \theta$ model. Ishida et al. previously developed a three-dimensional heat transfer analysis program to numerically analyse the temperature distribution of the dow-
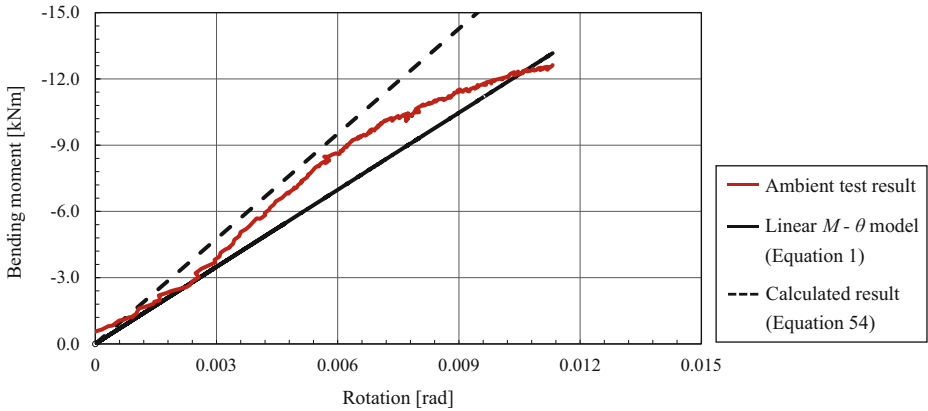
Figure 36. Comparison between ambient test result and calculated result.

els and the adjacent wood in the frame specimen. They reported that the experimental temperature distribution agreed well with the numerical temperature distribution [39]. The thermal properties recommended in Eurocode 5 [36] were utilized in the analysis. The numerical temperature distribution obtained by Ishida et al. was used to validate the non-linear $M - \theta$ model. Figure 38 shows the time history data for the temperature distribution. In reference [39], a comparison is made between the temperature distribution of the dowel and the wood 8 mm away from the surface of the dowel. According to the reference, the dowel temperature is higher near the steel plate, while the wood temperature is significantly higher near the beam surface. To consider the temperature distribution of the dowels and the charring of the adjacent wood, The time history data of the element temperatures utilized in the analysis corresponds to the maximum value between the dowel temperature and the temperature of the wood at a point 8 mm away from the surface of the dowel. Figure 37 compare the experimental fire test result of the right-side connection with the analytical results calculated by the non-linear $M - \theta$ model. Since the measurement of the $M - \theta$ relationship of the left-side connection was unstable, the $M - \theta$ relationship of the right-side connection was used to validate the non-linear $M - \theta$ model. The time history of the rotations, θ^t, required in the analysis (Eq. 16) was obtained from the test result calculated using Eq. (52) (Fig. 33). a_m of each dowel was always assumed to be 0 in the analysis because the dowels of the specimen connections were aligned vertically in a row.

As shown in Fig. 37, the non-linear $M - \theta$ model agreed well with the solid line during the pre-loading phase and until 50 min. The analytical result started to decrease after 50 min and agreed well with the dotted line in which the bending moment of the column was ignored. The time history data of the element temperatures used in the analysis is presented in Fig. 38. The temperature of all elements gradually increased as the heating progressed and exceeded 100°C between 60 and 70 min. Due to the slower reduction in the reduction factors of timber above
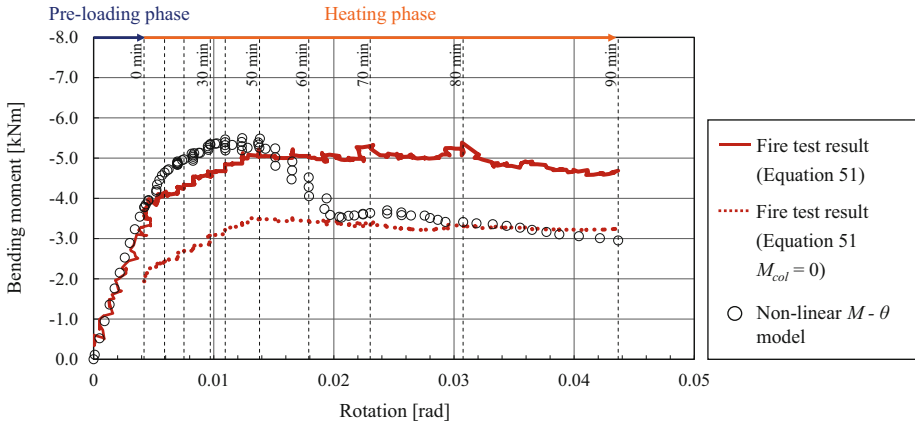
Figure 37. Comparison between fire test result and analytical result.
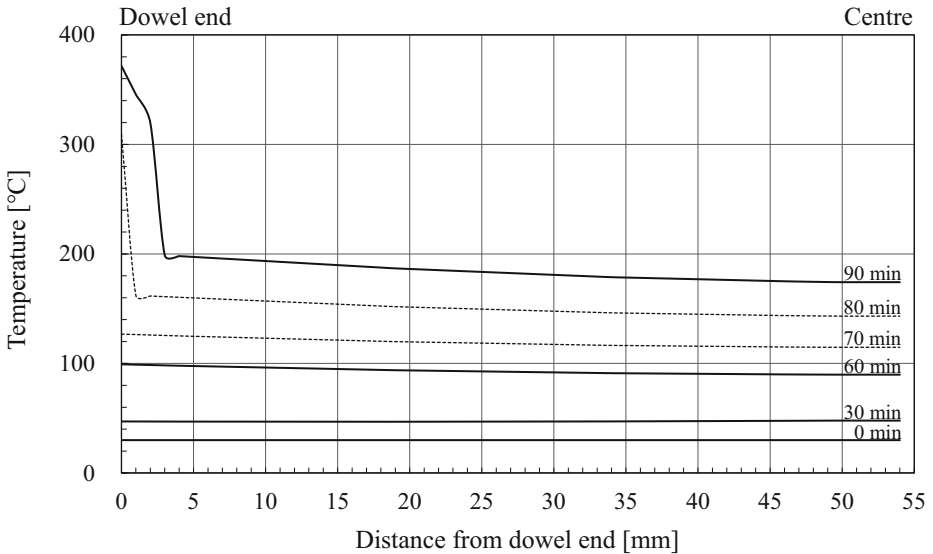

Figure 38. Time history of element temperatures.

100°C than below 100°C (as shown in Fig. 13), the analytical result decreased after 50 min, whereas they became almost constant after approximately 65 min. Considering the possibility that the experimental $M - \theta$ relationship is expected to be close to the solid line in the early stages of the fire and close to the dotted line in the ultimate stages of the fire, the non-linear $M - \theta$ model simulated the experimental $M - \theta$ behaviour with good accuracy. After 80 min, the analytical result
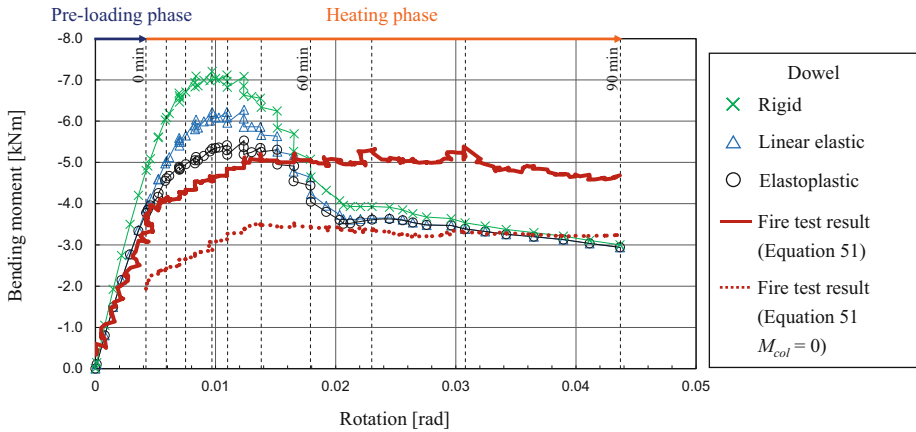
Figure 39. Comparison between the three analytical results.
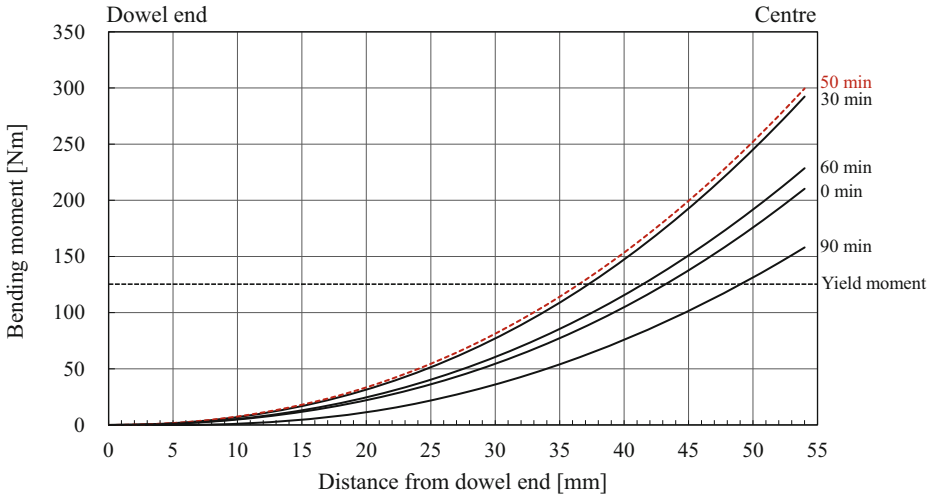

Figure 40. Bending moment diagram of the bottom dowel.

slightly fell below the dotted line, representing the lowest experimental result. This discrepancy can be attributed to the higher temperature near the dowel head used in the analysis (Fig. 38) compared to the temperature observed during the experiment (Fig. 22).

To examine the effect of varying the stress–strain relationship of the dowel, three analyses were performed, in which the relationship was assumed to be rigid, linear elastic, and elastoplastic. Figure 39 presents a comparison of the three

results. The other analysis conditions are the same as the analysis of the right-side connection. The rigid and linear elastic body assumption of the dowels overestimated the elastoplastic result until 65 min; interestingly, the three results converged to the same value after 65 min. This result suggests that the failure mode of the dowels was determined only by the embedding failure of timber, and not by the formation of plastic hinges. This phenomenon can be described in Fig. 40, which shows the bending moment distribution along the bottom dowel obtained through the analysis of the right-side connection (Fig. 37). As illustrated in Fig. 40, the centre of the dowel was plasticized at the end of the pre-loading phase. The bending moment distribution reached its peak at 50 min and monotonically declined thereafter as the stress on each element, calculated from Eq. (20), decreased. The decline in the bending moment distribution signifies that the stress–strain states of the plasticised elements entered their linear unloading phase (Case III in Eq. 29) after 50 min, and their bending stiffness recovered to elasticity, while the contacting timber was charred and plasticised. Accordingly, the dowel exhibited similar behaviour to that of a rigid body, and the plastic deformation in the pre-loading phase did not significantly develop during the fire. As a result, no significant residual deformation of the dowel was observed after the fire test, as shown in Fig. 27b. The convergence of the three results implies that the ultimate states of beams with dowel-type connections exposed to fire can be approximated by assuming that dowels are rigid bodies.

7. Conclusions

A theoretical model for the linear elastic $M - \theta$ relationships of dowel-type connections under ambient conditions was introduced (linear $M - \theta$ model). Subsequently, this model was applied to develop an analytical model for non-linear $M - \theta$ relationships of dowel-type connections exposed to fire (non-linear $M - \theta$ model). To validate the models, two load-bearing tests were performed on large-scale glulam frames, each under ambient and fire conditions, and the results obtained by the models were compared with the test results.

In the elastic range, the linear $M - \theta$ model provided satisfactory approximations of the measured $M - \theta$ relationships. The result obtained using the non-linear $M - \theta$ model agreed well with the $M - \theta$ relationship of the right-side connection in the fire test. The analytical result closely matched the fire test result for the right-side connection until 50 min, after which both the analytical and experimental results stabilized.

To examine the effect of varying the stress–strain relationship of the dowel, three analyses were performed using the non-lienar $M - \theta$ model, in which the relationship was assumed to be rigid, linear elastic, and elastoplastic. Interestingly, the three results showed little difference after 65 min as the stress–strain states of the plasticised elements entered their linear unloading phase, and their bending stiffness recovered to elasticity after 50 min. This result suggests that the ultimate states of beams with dowel-type connections exposed to fire can be approximated by assuming that dowels are rigid bodies.

8. Future Work

The non-linear $M - \theta$ model proposed in this study will be incorporated into the fire response analysis model for timber beams based on [4]. This installation will enable the simulation of fire behaviour of timber frames considering the semi-rigidity of dowel-type connections. The numerical results will be compared with the time–displacement relationship and fire-resistance time of the timber frame specimen obtained by the fire test introduced in this study.

Acknowledgements

Open Access

References

1. Okunrounmu O, Salem O, Hadjisophocleous G (2021) Fire performance of hybrid mass timber beam-end connections with perpendicular-to-wood grain reinforcement. J Struct Fire Eng. https://doi.org/10.1108/JSFE-06-2021-0036
2. Yotsumoto N, Kikuchi T, Kawarabayashi F, Nakayama Y, Totsuka M, Hirashima T (2022) Influence of dowel-type connections on fire resistance of structural glulam timber beams–part 4: results of loading tests at ambient temperature on Japanese Larch, summaries of technical papers of annual meeting, Architectural Institute of Japan, pp 125–126 (**in Japanese**)
3. Kikuchi T, Yotsumoto N, Kawarabayashi F, Nakayama Y, Totsuka M, Hirashima T (2022) Influence of dowel-type connections on fire resistance of structural glulam timber beams–part 5: results of the load-bearing fire tests on Japanese Larch, summaries of technical papers of annual meeting, Architectural Institute of Japan, 2022, pp 127–128 (**in Japanese**)

4. Becker J, Bresler B (1974) A computer program for the fire response of structures-reinforced concrete frames. Fire Research Group, University of California, Berkley
5. da Silva LS, Santiago A, Real PV (2001) A component model for the behaviour of steel joints at elevated temperatures. J Constr Steel Res 1(11):1169–1195
6. Sarraj M (2007) The behavior of steel fin plate connections in fire, Sheffield University, Ph. D. Thesis
7. Kuenzi EW (1955) Theoretical design of a nailed or bolted joint under lateral load, Forest Products Laboratory, Forest Service, United States Department of Agriculture, Madison, USA
8. Hirai T, Sawada M (1982) Linear load-slip relationship of bolted joints of glued-laminated lumber. Mokuzai Gakkaishi 28(10):609–613
9. Hirai T, Sawada M (1982) Nominal bearing stresses of bolted wood-joints at apparent proportional-limits. Mokuzai Gakkaishi 28(9):543–547
10. Girhammar UA, Jacquier N, Källsner B (2017) Stiffness model for inclined screws in shear-tension mode in timber-to-timber joints. Eng Struct 136:580–595. https://doi.org/10.1016/j.engstruct.2017.01.022
11. Tao H, Yang H, Ju G, Shi B (2021) Elastic stiffness of timber joints with dowel-type fasteners and slotted-in steel plate based on the theory of beam on elastic foundation. Constr Build Mater. https://doi.org/10.1016/j.conbuildmat.2021.123569
12. Tsujino T, Hirai T (1983) Nonlinear load-slip relationship of bolted wood-joints with steel side-members I. Numerical analysis based upon a finite element method. Mokuzai Gakkaishi 29(12):833–838 **(in Japanese)**
13. Hirai T (1983) Nonlinear load-slip relationship of bolted wood-joints with steel side-members II. Application of the generalized theory of a beam on an elastic foundation. Mokuzai Gakkaishi 29(29):839–844
14. Hirai T (1985) Nonlinear load-slip relationship of bolted wood-joints with steel side-members III. Advanced numerical analysis based on the generalized theory of a beam on an elastic foundation. Mokuzai Gakkaishi 31(3):165–170
15. Foschi RO (1974) Load-slip characteristics of nails. Wood Science 7:69–76
16. Awaludin A, Smittakorn W, Hayashikawa T, Hirai T (2007) M-θ curve of timber connection with various bolt arrangements under monotonic loading. J Struct Eng 53A:853–862
17. Yasuda Y, Inayama M, Aoki K, Soma T (2016) Verification of approximate analysis by beam-model for the load–slip characteristics of drift-pinned joints with the steel plate inserted. J Struct Constr Eng 81(727):1501–1511. https://doi.org/10.3130/aijs.81.1501 **(in Japanese)**
18. Yasuda Y, Aoki K, Inayama M (2018) Comparison of the test and analysis of moment-resisting joint – verification of approximate analysis by beam-model for the load-slip characteristics of drift-pinned joints with the steel plate inserted part. J Stust Constr Eng 83(744):275–283. https://doi.org/10.3130/aijs.83.275. **(in Japanese)**
19. Architectural Institute of Japan (2015) Design manual for engineered timber joints (**in Japanese**)
20. Cachim PB, Franssen JM (2009) Numerical modelling of timber connections under fire loading using a component model. Fire Saf J 44:840–853. https://doi.org/10.1016/j.firesaf.2009.03.013
21. Erchinger C, Frangi A, Fontana A (2010) Fire design of steel-to-timber dowelled connections. Eng Struct 32:580–589. https://doi.org/10.1016/j.engstruct.2009.11.004
22. Audebert M, Dhima D, Taazount M, Bouchaïr A (2011) Numerical investigations on the thermo-mechanical behavior of steel-to-timber joints exposed to fire. Eng Struct 33:3257–3268. https://doi.org/10.1016/j.engstruct.2011.08.021

23. Audebert M, Dhima D, Taazount M, Bouchaïr A (2012) Behavior of dowelled and bolted steel-to-timber connections exposed to fire. Eng Struct 39:116–125. https://doi.org/10.1016/j.engstruct.2012.02.010
24. Audebert M, Dhima D, Taazount M, Bouchaïr A (2013) Thermo-mechanical behaviour of timber-to-timber connections exposed to fire. Fire Saf J 56:52–64. https://doi.org/10.1016/j.firesaf.2013.01.007
25. Audebert M, Dhima D, Taazount M, Bouchaïr A (2014) Experimental and numerical analysis of timber connections in tension perpendicular to grain in fire. Fire Saf J 63:125–137. https://doi.org/10.1016/j.firesaf.2013.11.011
26. Palma P, Frangi A, Hugi E, Cachim P, Cruz H (2016) Fire resistance tests on timber beam-to-column shear connections. J Struct Fire Eng 7(1):41–57. https://doi.org/10.1108/JSFE-03-2016-004
27. Racher P, Laplanche K, Dhima D, Bouchaïr A (2010) Thermo-mechanical analysis of the fire performance of dowelled timber connection. Eng Struct 32:1148–1157. https://doi.org/10.1016/j.engstruct.2009.12.041
28. Peng L, Hadjisophocleus G, Mehaffey J, Mohammad M (2011) Predicting the fire resistance of wood–steel–wood timber connections. Fire Technol 47:1101–1119. https://doi.org/10.1007/s10694-009-0118-4
29. Palma P, Frangi A (2019) Modelling the fire resistance of steel-to-timber dowelled connections loaded perpendicularly to the grain. Fire Saf J 107:54–74. https://doi.org/10.1016/j.firesaf.2017.12.001
30. Dhima D, Audebert M, Bouchaïr A (2014) Analysis of the thermos-mechanical behaviour of steel-to-timber connections in bending. J Struct Fire Eng 5(2):97–112
31. Li Z, Luo J, He M, He G, Sun Y (2021) Analytical prediction of the fire resistance of the glulam bolted connections under coupled moment and shear. J Build Eng. https://doi.org/10.1016/j.jobe.2020.101531
32. Luo J, Li Z, He M, Gan Z, Wang X (2022) Analytical investigation and parametric study on the fire behavior of glulam bolted beam-to-column connections based on the quasi-non-linear fracture mechanics model. Fire Saf J. https://doi.org/10.1016/j.firesaf.2022.103662
33. Luo J, He M, Li Z, Gan Z, Wang X, Liang F (2022) Experimental and numerical investigation into the fire performance of glulam bolted beam-to-column connections under coupled moment and shear force. J Build Eng. https://doi.org/10.1016/j.jobe.2021.103804
34. EN 1993-1-1 (2005) Eurocode 3: design of steel structures—Part 1–2: General rules–structural fire design
35. Kawarabayashi F, Kikuchi T, Totsuka M, Hirashima T (2022) Embedding behaviors of a dowelled connection in structural glulam timbers at high temperature. J Stuct Constr Eng 87(795):498–509. https://doi.org/10.3130/aijs.87.498 **(in Japanese)**
36. EN 1995-1-2 (2004) Eurocode 5: Design of timber structures–Part 1–2: General–Structural fire design
37. Kikuchi T, Yotsumoto N, Kawarabayashi F, Ishida Y, Totsuka M, Hirashima T (2023) Experimental study on fire performance of glulam timber frames–Part 1: Temperatures and charring behavior of the beam–column connections exposed to standard fire heating for more than 1 hour. J Strus Constr Eng 87(802):1300–1311. https://doi.org/10.3130/aijs.87.1300 **(in Japanese)**
38. Architectural Institute of Japan (2006) Standard for structural design of timber structures (**in Jananese**)

39. Ishida Y, Hirashima T, Totsuka M (2022) Three-dimensional heat transfer analysis of dowelled type connections for timber structures, summaries of technical papers of annual meeting, Architectural Institute of Japan, 2022, pp 159–162 (**in Japanese**)